Preparation and Characterization of a Formally Ni^{IV}-Oxo Complex with a Triplet Ground State and Application in Oxidation Reactions

Deepika G. Karmalkar,[a,†] Virginia A. Larson,[b,†] Deesha D. Malik,[a] Yong-Min Lee,[a] Mi Sook Seo,[a] Jin Kim,[a] Dovydas Vasiliauskas,[c] Jason Shearer,[c,*] Nicolai Lehnert,[b,*] and Wonwoo Nam[a,*]

[†] D.G.K. and V.A.L. are co-first authors.

[a] Department of Chemistry and Nano Science, Ewha Womans University, Seoul 03760, Korea;

[b] Department of Chemistry and Department of Biophysics, University of Michigan, Ann Arbor, Michigan 48109-1055, United States

[c] Department of Chemistry, Trinity University, San Antonio, Texas 78212-7200, United States

Corresponding Authors

Jason Shearer − Department of Chemistry, Trinity University, San Antonio, Texas 78212-7200, United States; orcid.org/0000-0001-7469-7304; Email: jshearer@trinity.edu

Nicolai Lehnert − Department of Chemistry and Department of Biophysics, University of Michigan, Ann Arbor, Michigan 48109-1055, United States; orcid.org/0000-0002-5221-5498; Email: lehnertn@umich.edu

Wonwoo Nam − Department of Chemistry and Nano Science, Ewha Womans University, Seoul 03760, Korea; orcid.org/0000-0001-8592-4867; Email: wwnam@ewha.ac.kr

Authors

Deepika Karmalkar – Department of Chemistry and Nano Science, Ewha Womans University, Seoul 03760, Korea; orcid.org/0000-0001-7386-6989

Virginia A. Larson − Department of Chemistry and Department of Biophysics, University of Michigan, Ann Arbor, Michigan 48109-1055, United States; orcid.org/0000-0002-7094-6286

Deesha D. Malik − Department of Chemistry and Nano Science, Ewha Womans University, Seoul 03760, Korea; orcid.org/0000-0001-7800-8852

Yong-Min Lee − Department of Chemistry and Nano Science, Ewha Womans University, Seoul 03760, Korea; orcid.org/0000-0002-5553-1453

Mi Sook Seo − Department of Chemistry and Nano Science, Ewha Womans University, Seoul 03760, Korea; orcid.org/0000-0003-3302-2508

Jin Kim – Department of Chemistry and Nano Science, Ewha Womans University, Seoul 03760, Korea; orcid.org/0000-0003-4006-8897

Dovydas Vasiliauskas − Department of Chemistry, Trinity University, San Antonio, Texas 78212-7200, United States

Abstract

High-valent first row transition metal-oxo complexes are important intermediates in biologically and chemically relevant oxidative transformations of organic molecules and in the water splitting reaction in (artificial) photosynthesis. While high-valent Fe- and Mn-oxo complexes have been characterized in detail, much less is known about their analogs with late transition metals. In this study, we present the synthesis and detailed characterization of a unique mononuclear terminal Ni–O complex. This compound, $[Ni(TAML)(O)(OH)]^{3-}$, is characterized by an intense charge-transfer (CT) band around 730 nm and has an S_t = 1 ground state, as determined by MCD spectroscopy. From EXAFS, the Ni–O bond distance is 1.84 Å. Ni K edge XAS data indicate that the complex contains a Ni(III) center, which results from an unusually large degree of Ni–O π-bond inversion, with one hole located on the oxo ligand. The complex is therefore best described as a low-spin Ni(III) complex (S = 1/2) with a bound oxyl ($O^{\bullet -}$) ligand (S = 1/2), where the spins of the Ni and the oxyl are ferromagnetically coupled, giving rise to the observed S_t = 1 ground state. This bonding description is roughly equivalent with the presence of a Ni–O single (σ) bond. Reactivity studies show that $[Ni(TAML)(O)(OH)]^{3-}$ is a strong oxidant capable of oxidizing thioanisole and styrene derivatives with large negative ρ values in the Hammett plot, indicating its electrophilic nature. The intermediate also shows high reactivity in C-H bond activation of hydrocarbons with a KIE of 7.0(3) in xanthene oxidation.

1. Introduction

High-valent first-row transition metal-oxo species are active intermediates in oxidation reactions that are important in biology, oxidative chemical transformations, and water splitting for the generation of renewable energy carriers.[1,2] Fe- and Mn-oxo species are active intermediates in enzymes like Cytochrome P450s, methane monooxygenase, mononuclear non-heme iron enzymes, and photosystem II, to name a few examples.[3,4] While Fe, Mn, and Cu are the favored metals for biology – high-valent Cu intermediates have been proposed for some enzymes but are less studied[5–7] – outside of bioinorganic chemistry, similar species with other transition metals have been used in chemical oxidation reactions, i.e. oxygen atom transfer (OAT) and C-H activation.[8–13] Metal-oxo moieties are also relevant for renewable energy related reactions, like the oxidative side of water splitting, referred to as the oxygen evolution reaction (OER), and the reduction of O_2 to water in fuel cells.[14–18] A notable example of the latter is Nocera's artificial leaf, which catalyzes the OER via a high-valent Co-oxo intermediate.[19] Additionally, though more recently developed, there are several molecular Ni OER catalysts that likely also operate through high-valent Ni–O intermeditates.[18]

Well studied, mononuclear, terminal Ni-oxo complexes are much more rare than their lower atomic number counterparts.[1,20] This is related to the concept of the 'oxo wall'.[21–23] A metal-oxo bond results from overlap of the metal(d) and the oxygen(p) orbitals. As one moves from left to right in the periodic table, for a particular metal oxidation state, the metal gains further d-electrons which populate the antibonding π* and σ* orbitals of the metal-oxo bond. Populating antibonding orbitals lessens the formal M–O bond order, destabilizing the species. Specifically, with low-spin M^{IV}-oxo species in tetragonal C_{4v} symmetry, a formal M–O double bond (bond order of 2) is not possible past iron. This is referred to as the 'oxo wall' and is explained in more detail in a number of review articles.[1,22] Nickel is past this 'oxo wall', having two additional metal(d) electrons compared with iron. This makes corresponding Ni^{IV}-O complexes extremely unstable and reactive. A Ni^{IV}–O complex in the low-spin (S_t = 0) state has a formal bond order of 1, which would not qualify as a metal=O unit. In addition, a metal-oxyl species may be expected, where bond inversion (valence tautomerization) gives rise to a radical on the oxo ligand. However, with intermediate (S_t = 1) or high-spin (S_t = 2) ground states, it is theoretically possible to have a formal Ni–O bond order of up to 1.5. This spin-state dependent Ni^{IV}-O bond order is illustrated in Scheme 1.

In line with this predicted instability, high-valent Ni-O species are rare in the literature. Some reports propose these types of species as intermediates for reactions like olefin epoxidation,[24,25] alkane hydroxylation,[26] and for gas phase methane oxidation to methanol (Scheme 2A, B).[27,28] Even in these cases, the involvement of a high-valent Ni–O species is debated.[29,30] For example, isotopic labeling and selectivity studies suggest that a *m*-chlorobenzoyloxy radical is the active species in C-H activation when *m*-chloroperbenzoic acid (*m*-CPBA) is reacted with nickel complexes featuring a variety of nitrogen-based coligands and appropriate substrates for C-H activation.[29] Nevertheless, high-valent Ni-O species have great potential as catalysts, and there is great interest in the field in isolating and understanding these reactive intermediates.[1,31]

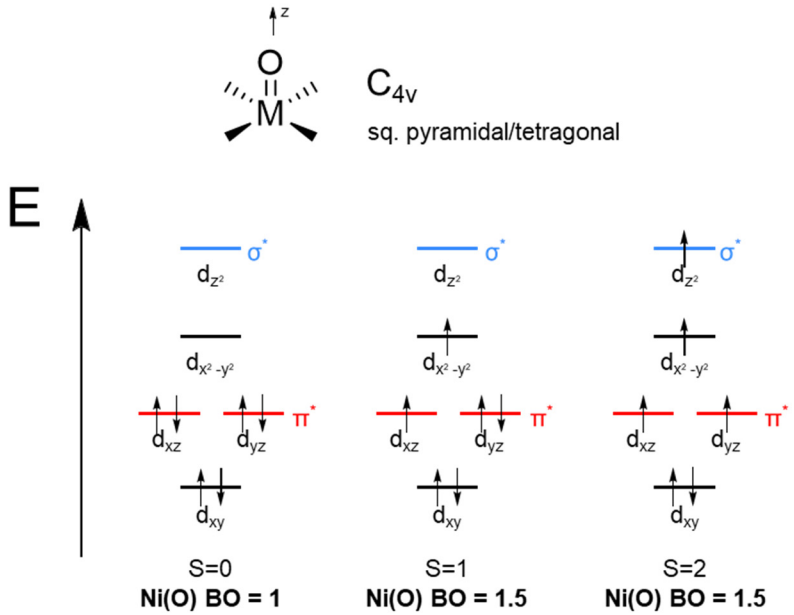

Scheme 1. Electronic structure of Ni-oxo complexes in different spin states and the resulting formal Ni–O bond order, illustrating the instability of metal-oxo species past the 'oxo wall'.

To date, only a few high valent Ni–O species have been proposed and/or successfully synthesized and characterized, as shown in Scheme 2. General strategies to obtain these species mirror those used for other types of metal-oxo complexes. This includes, in particular, the reaction of Ni(II) precursors with O-atom transfer reagents like *m*-CPBA, as first reported in 2012 by Ray and co-workers.[32] Here, reaction of a Ni^{II} precursor, $[Ni^{II}(TMG_3tren)(OTf)]^+$, with *m*-CPBA yielded $[Ni^{III}(TMG_3tren)(O \text{ or } OH))(OTf)]^{1+ \text{ or } 2+}$ in 15% yield, distributed across two isomers (Scheme 2C). Characterization by EPR revealed two rhombic S_t = 1/2 species consistent with a Ni-O or Ni-OH complex, and UV-Vis spectroscopy showed a new band at 520 nm for these intermediates. Both isomers were deemed reactive for OAT and C-H activation. In 2015, Company and co-workers reported a $[Ni^{III}(L)(O^{\bullet})]$ complex, which was described as a Ni^{III}-oxyl species (Scheme 2D, H_2L = 6-methyl-3,6,9-triaza-1(2,6)-pyridinacyclodecaphane-2,10-dione).[33] This EPR-silent species was characterized by UV-Vis and rRaman spectroscopy, XANES, and EXAFS, the latter indicating a rather long Ni–O bond distance of 2.12 Å. Finally, a mix of $Ni^{IV}(O)$ and $Ni^{III}(O)$ species was reported by Kim and co-workers in 2016 as intermediates in the catalytic epoxidation of olefins by $[Ni^{II}(dpaq)Cl]$ treated with the oxidant *m*-CPBA (Scheme 2E).[34] Since our 2020 review, there have been a few proposed Ni(O) intermediates,[35–38] but these lack in depth spectroscopic characterization. Recently, O-NiF_2 has been prepared in a solid neon matrix by Riedel and co-workers. Here, a $^{16/18}O$-sensitive band was observed in IR spectroscopy at 640 cm^{-1} and assigned to the Ni-F_2 symmetric stretch with some influence of the adjacent O. This species was further concluded, based on CASSCF/CASTP2/VTZ-DK calculations, to have a strong degree of oxyl character in the ground state (Scheme 2F).[39] Despite the interest in mononuclear, terminal Ni–O species and aforementioned in-depth studies of these reactive and unstable intermediates, there is still no direct spectroscopic evidence for a Ni-O bond other than in O–NiF_2.

In this paper, we report the synthesis, spectroscopic characterization, and reactivity of a formally $Ni^{IV}(O)$(TAML) ($TAML^{4-}$ = tetraamido macrocyclic ligand) complex, which has a near

tetragonal ligand field symmetry. UV-Vis, XAS, and MCD spectroscopic and EXAFS studies show that this species corresponds to a six-coordinate formally Ni^{IV}-O complex with an axially-coordinated hydroxide ligand and an S_t = 1 ground state. We further analyze the electronic structure of this complex, using experimentally calibrated DFT calculations, which show a distinct amount of bond inversion for one of the Ni–O π-bonds, giving this complex dominant Ni^{III}-oxyl character. The proposed structure of this species is shown in Scheme 2G. Finally, the reactivity of this complex with respect to C-H bond activation and OAT is investigated, including full kinetic analyses. Our data show that $[Ni(TAML)(O)(OH)]^{3-}$ is a particularly active catalyst for the OAT reaction and that this species can activate moderately strong C-H bonds. The reactivity of the Ni intermediate in oxidation reactions is summarized in this paper.

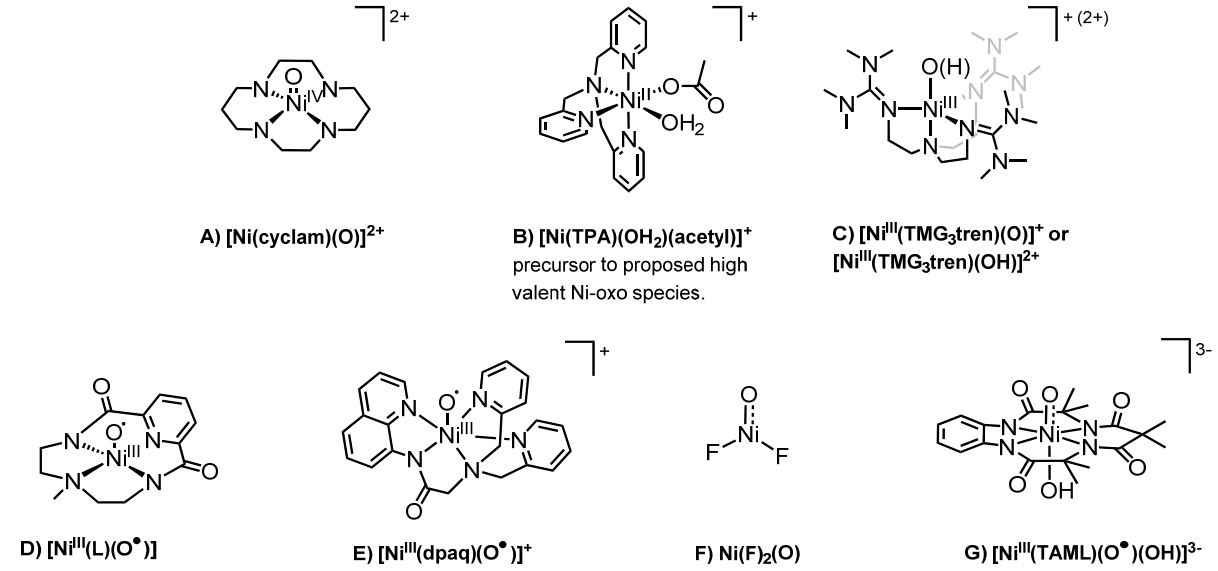

Scheme 2. Previously reported Ni–O complexes (A – F) and $[Ni(TAML)(O)(OH)]^{3-}$ (G) presented in this paper. H_2L = 6-methyl-3,6,9-triaza-1(2,6)-pyridinacyclodecaphane-2,10-dione.

2. Results and Analysis

2.1. Synthesis and Characterization of $[Ni^{II}(TAML)]^{2-}$ (1) and $[Ni^{III}(TAML)]^{-}$ (2).

The Ni(II) complex $[Ni^{II}(TAML)]^{2-}$ (**1**) was synthesized by reaction of deprotonated ligand, $TAML^{4-}$ ($TAML^{4-}$ = tetraamido marcrocyclic ligand, 3,4,8,9-tetrahydro-3,3,6,6,9-hexamethyl-1*H*-1,4,8,11-benzotetraazocyclotridecane-2,5,7,10-(6*H*,11*H*)-tetrone) with 1.2 equiv of $[Ni^{II}(acac)_2]$ in dry THF under an argon atmosphere[40] (see Experimental Section for the detailed synthetic procedure). **1** shows an electronic absorption band at 435 nm (ε = 60 M^{-1} cm^{-1}) in acetonitrile (MeCN; Supporting Information (SI), Figure S1a). Cold-spray ionization mass spectrometry (CSI-MS) of **1** shows a prominent ion peak in negative mode at a mass to charge ratio of *m/z* = 435.1 (Figure S1b), whose mass and isotope distribution pattern correspond to $Li[Ni^{II}(TAML)]^{-}$ (calcd. *m/z* = 435.1). The X-band electron paramagnetic resonance (EPR) spectrum of **1** along with the Evans method using ^1H NMR experiments revealed that **1** is a diamagnetic complex with S_t = 0 spin state (Figure S1c). Crystals of **1** suitable for X-ray crystallographic measurements were obtained by layering a MeCN solution of **1** with Et_2O at room temperature (see Experimental Section for more details). On collection of crystal data and structural refinement, the crystals were determined

to be a $[Ni^{II}(TAML)]^{2-}$ complex with a Ni-N_{avg} bond length of 1.839(2) Å (Figure S2, Tables S1 − S2).

The Ni(III) complex $[Ni^{III}(TAML)]^{-}$ (**2**) was generated by using a one-electron oxidant such as cerium(IV) ammonium nitrate (CAN). **2** was synthesized by reacting **1** with 1 equiv of CAN in MeCN at 25 °C. **2** shows electronic absorption bands at 730 and 1030 nm (ε = 1800 and 3200 M^{-1} cm^{-1}, respectively) in MeCN (Figure S3a). A titration experiment showed that 1 equiv of CAN is required for the full conversion of **1** to **2** (Figure S3a, inset). CSI-MS of **2** shows a prominent ion peak in negative mode at a mass to charge ratio of *m/z* = 428.1 (Figure S3b), whose mass and isotope distribution pattern correspond to $[Ni^{III}(TAML)]^{-}$ (calcd. *m/z* = 428.1). The X-band EPR spectrum of **2** revealed that **2** is a paramagnetic complex with S_t = 1/2 spin state, having *g* values at 2.20, 2.07, and 1.99 (Figure S3c). The S_t = 1/2 spin state of **2** was confirmed by Evans method using ^{1}H NMR experiments. Crystals of **2** suitable for X-ray crystallographic measurements were obtained by layering an acetonitrile solution of **2** with Et_2O at −20 °C (see Experimental Section for more details). On collection of crystal data and structural refinement, the crystals were determined to be the $[Ni^{III}(TAML)]^{-}$ complex with a Ni-N_{avg} bond length of 1.825(2) Å (Figure S4, Tables S3 − S4).

2.2. Synthesis and Basic Characterization of $[Ni(TAML)(O)(OH)]^{3-}$ (3).

The formally Ni(IV)-oxo-hydroxo complex $[Ni(TAML)(O)(OH)]^{3-}$ (**3**) was generated by reacting **1** with 2 equiv of CAN (or by reacting **2** with 1 equiv of CAN) in the presence of H_2O (5.0 µL) in MeCN at −40 °C. When **1** was reacted with 2 equiv of CAN, a distinct color change was observed from yellow (starting) to bright blue within few seconds. **3** shows a prominent electronic absorption band at 728 nm (ε = 4000 M^{-1} cm^{-1}) in MeCN (Figure 1a, also see Figure S5). A titration experiment showed that 1 equiv of CAN is required for the full conversion of **2** to **3** (Figure 1a, inset). Alternatively, **3** can also be generated by reacting **1** with 1.5 equiv of PhIO (dissolved in trifluoroethanol (TFE)), followed by addition of 1 equiv of trifluoromethanesulfonic acid (HOTf) in MeCN at −40 °C (Figure S6).

Complex **3** is metastable at −40 °C ($t_{1/2}$ ~3 h), which allowed us to characterize it with various spectroscopic techniques. CSI-MS of **3** shows poor intensity in positive and negative mode under above conditions. In order to trap the intermediate using CSI-MS, 1 equiv of inactive metal triflates, such as zinc triflate $[Zn(OTf)_2]^{2+}$, was added to a solution of **3**, generated using PhIO in the presence of HOTf in MeCN:TFE (*v/v* = 1:1) at –40 °C. The peak at a mass to charge ratio of *m*/*z* = 445.2 in positive mode was assigned to be $\{H^+ + [Ni(TAML)(O)]\}$ (calcd. *m*/z = 445.2), with isotope distribution pattern for Ni-oxygen species. When **3-^{18}O** was used, a two-mass unit shift was observed at *m*/z = 447.2 (Figure 1b). The observation of the two-mass unit shift upon ^{18}O-introduction indicates that **3** contains one isotope sensitive oxygen atom.

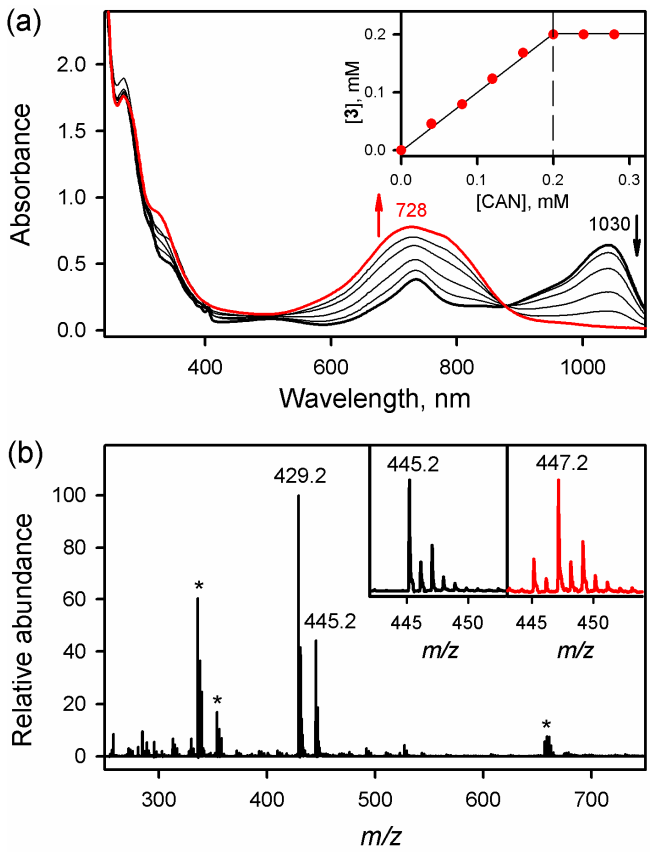

Figure 1. (a) UV-Vis spectral changes showing the formation of **3** in the reaction of **2** (0.20 mM) with CAN (0 – 0.20 mM) in MeCN at –40 °C. The inset shows titration data of $[Ni^{III}(TAML)]^-$ (0.20 mM) with CAN (0 – 0.28 mM). (b) CSI-MS spectra of **3** in positive ion mode. The peaks at *m/z* = 445.2 correspond to $\{H^+ + [Ni(O)(TAML)]\}$ (calcd. *m/z* = 445.1). Inset shows the observed isotope distribution pattern for **3**-^{16}O (left panel) and **3**-^{18}O (right panel). The peaks marked with an asterisk (*) originate from zinc triflate, $Zn(OTf)_2$, $\{Na^+ + [Zn(OTf)(CF_3CH_2OH)]\}$, (*m/z* = 336.0) and $\{Na^+ + [Zn(OTf)(CF_3CH_2OH)(H_2O)]\}$, *m/z* = 354.0).

The X-band EPR spectrum of **3**, measured at 5K, is silent (Figure S7a). In contrast, the EPR spectrum of $[Ni^{III}(TAML)]^-$ shows signals around $g \sim 2$ (see above), while its one-electron oxidized species, equivalent to **3**, shows no EPR signal (EPR spectra of **2** and **3** are compared in Figure S7b). This reveals that the oxidation state of **3** is consistent with a formally +4 species, one oxidation state higher than that of the Ni(III) complex **2**. To confirm the oxidation state of **3,** reduction of **3** was carried out using ferrocene derivatives. Addition of 1 equiv of ferrocene (Fc) to **3** led to the formation of the one-electron reduced species, $[Ni^{III}(TAML)]^-$ (**2**), and addition of 2 equiv of decamethylferrocene ($Me_{10}Fc$) to **3** gave rise to its two-electron reduced species, $[Ni^{II}(TAML)]^{2-}$ (**1**). The formation of the reduced species from **3** was confirmed using UV-Vis and EPR experiments (Figure S8). The oxidation state of **3** was also confirmed by cyclic voltammetry (Figure S9). The cyclic voltammogram (CV) of $[Ni^{II}(TAML)]^{2-}$ (**1**) in MeCN/H_2O (v/v 19:1) displays two reversible oxidation waves at $E_{1/2}$ vs SCE = 0.19 and 0.85 V (Figure S9a). The second-electron oxidation potential (E_{ox} = 0.85 V vs SCE) of **1** is the same as the one-electron reduction potential of Ni-oxyl (**3**) species (E_{red} = 0.85 V vs SCE), which was generated by reacting **1** (2.0 mM) with CAN (2.0 equiv) in MeCN/H_2O (v/v 19:1) at −40 °C (Figure S9b). It should be noted that

3 undergoes a comproportionation reaction with **1**, leading to the formation of $[Ni^{III}(TAML)]^-$ in stoichiometric yield (Figure S10). For a formally d^6 Ni^{IV} species, this means that the $Ni^{IV}(O)$ unit could be high-spin (S_t = 2), intermediate spin (S_t = 1), or low-spin (S_t = 0). The question of the spin state is addressed using MCD spectroscopy (see below), which demonstrates that the species associated with the 728 nm absorption feature has an S_t = 1 ground state. Following the synthesis of intermediate **3**, a variety of characterization techniques were used to determine its geometric and electronic structure.

2.3. X-ray Absorption Spectroscopy and Analysis.

To determine the coordination environment and metric parameters associated with **3** we examined cryogenic solutions of **3** by nickel K-edge X-ray absorption spectroscopy. We note that samples of **3** are highly susceptible to photoreduction, and even with significant X-ray beam attenuation the beam had to be moved after every scan owing to photodamage of the sample. The XANES region of the Ni K-edge X-ray absorption spectra for **1**, **2**, and **3** are depicted in Figure 2a. All three complexes display a weak Ni(1s → 3d) feature at ~8331 eV signifying that the three complexes contain nickel in a centrosymmetric ligand environment (i.e. four-coordinate square-planar or six-coordinate quasi-octahedral). Complexes **1** and **2** display a prominent feature at ~8335 eV, which is assigned as a Ni(1s → $4p_z$) transition. Such a feature is characteristic of square planar nickel-centers, as this feature significantly blue-shifts into the edge upon coordination of axial ligands. It is noteworthy that this feature is lacking for **3**, signifying that Ni is not contained in a four-coordinate square planar ligand environment in this case, but is instead contained in a six-coordinate ligand environment. Furthermore, the weak pre-edge feature is inconsistent with a short axial oxo ligand as has been observed in other metal-oxo complexes generated to date – a short Ni-O bond (1.60 – 1.75 Å) would be expected to generate a more intense pre-edge feature. This is fully supported by simulations of the pre-edge region of the Ni K-edge X-ray absorption spectrum using TD-DFT methods; the pre-edge features of **3** can only be reproduced using six-coordinate models with axial Ni-O bond lengths longer than 1.8 Å (Figure S11). The edge position of **3** is also not consistent with a Ni^{IV} center. The edge displays only a 0.8(2) eV blue shift from **1**, which contains a formal Ni^{II} center, and no shift relative to **2**, which contains a formal Ni^{III} center. Therefore, the oxidation state of nickel in **3** is most consistent with a formal Ni^{III} center.

The unfiltered and magnitude FT k^3 EXAFS spectrum of **3** is depicted in Figure 2b. Owing to extensive photodamage of the samples upon prolonged beam exposure, data could only be modeled out to a k = 13 $Å^{-1}$, which limited the resolution of two similar scatterers to a Δr = 0.14 Å.[41] Solutions to the EXAFS region are consistent with a six-coordinate nickel center. The data are best modeled with four Ni-N scatterers at 1.96 Å, one Ni-O scatterer at 1.84 Å, and one long Ni-O scatterer at 2.2 Å.[42] These three inner-sphere shells are therefore within the resolution of the experimental data. We note that the longer Ni-O scatterer is reasonably disordered (σ^2 = 0.008 $Å^{-2}$) suggesting it may be an artifact in the data fitting. However, if this shell is omitted from the refinements and included in either the Ni-O or the Ni-N shell, the resulting model yields unreasonably large Debye-Waller factors for that shell and an increase in both the Ni-O (to ~1.9 Å) and Ni-N distances (> 2.0 Å). The data are therefore most consistent with a Ni^{III} center coordinated by the TAML amidate nitrogen atoms, a short axial O or OH ligand and a longer axially-coordinated ligand.

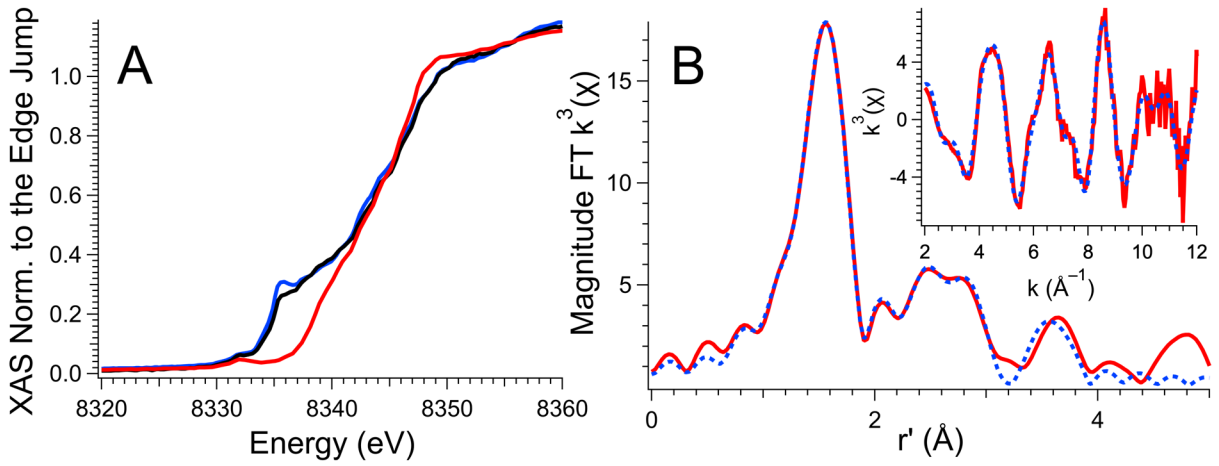

Figure 2. A: XANES region of the Ni K-edge spectra for **1** (blue), **2** (black), and **3** (red). B: Magnitude FT k^3 EXAFS spectrum of **3** with the experimental spectrum depicted as the solid red line and the best fit as the blue dashed line. The inset displays the k^3 EXAFS data of **3** with the experimental data depicted as the solid red line and the best fit as the blue dashed line. Best Fit: E_o = 8336.2 eV; Shell #1 (Ni-N): n = 4, r = 1.964(8) Å, σ^2 = 0.0029(7) Å^{-2}; Shell #2 (Ni-O): n = 1, r = 1.841(15) Å, σ^2 = 0.004(2) Å^{-2}; Shell #3 (Ni-O): n = 1, r = 2.24(2) Å, σ^2 = 0.0083(17) Å^{-2}; Shell #4 (Ni-C): n = 3.4(1), r = 2.875(5) Å, σ^2 = 0.0093(7) Å^{-2}; Shell #5 (Ni-C): n = 2.2(1), r = 3.143(5) Å, σ^2 = 0.0059(6) Å^{-2}; Shell #6 (Ni-C): n = 2.3(1), r = 3.996(10) Å, σ^2 = 0.0080(13) Å^{-2}. ε^2 = 0.81.

2.4. Magnetic Circular Dichroism Spectroscopy.

MCD spectroscopy was further used to understand the electronic structure of intermediate **3**, to determine the spin state of this species (since MCD **C**-term intensity is obtained for all paramagnetic species, including integer spin species,[43–47] unlike EPR), and to assign its optical data. Figure 3 shows a comparison of the UV-Vis and low-temperature MCD data of **3**. As shown Figure 3, the characteristic UV-Vis feature of **3** at 728 nm is also present in the MCD data, and hence, a fit of the variable-temperature variable-field (VTVH) MCD data obtained for this band provides direct insight into the magnetic properties of **3**, especially its spin state (see below). A correlated Gaussian fit of the UV-Vis and MCD data shown in Figure 3 identifies seven electronic transitions in the optical spectra, as listed in Table 1. Our results show that the feature at 728 nm actually corresponds to three different electronic transitions, bands 1 – 3, located at 12440, 13540 and 15080 cm^{-1}. Here, band 2 is the dominant feature in the MCD data, indicating that this transition involves a significant amount of metal character, and likely corresponds to either a d-d or a charge-transfer (CT) transition. To higher energy, bands 4 – 6 at 18440, 20580 and 23960 cm^{-1} are quite intense in the absorption but weak in the MCD spectrum, suggesting that these could be ligand-based transitions. Finally, band 7 is again intense both in the UV-Vis and MCD data, and could originate from a second CT transition. Further insight into the assignments of bands 2 and 7 can be obtained from the analysis of the VTVH data of these features. Unfortunately, the other optical features are too weak in the MCD spectra to obtain reliable VTVH data for further analysis.

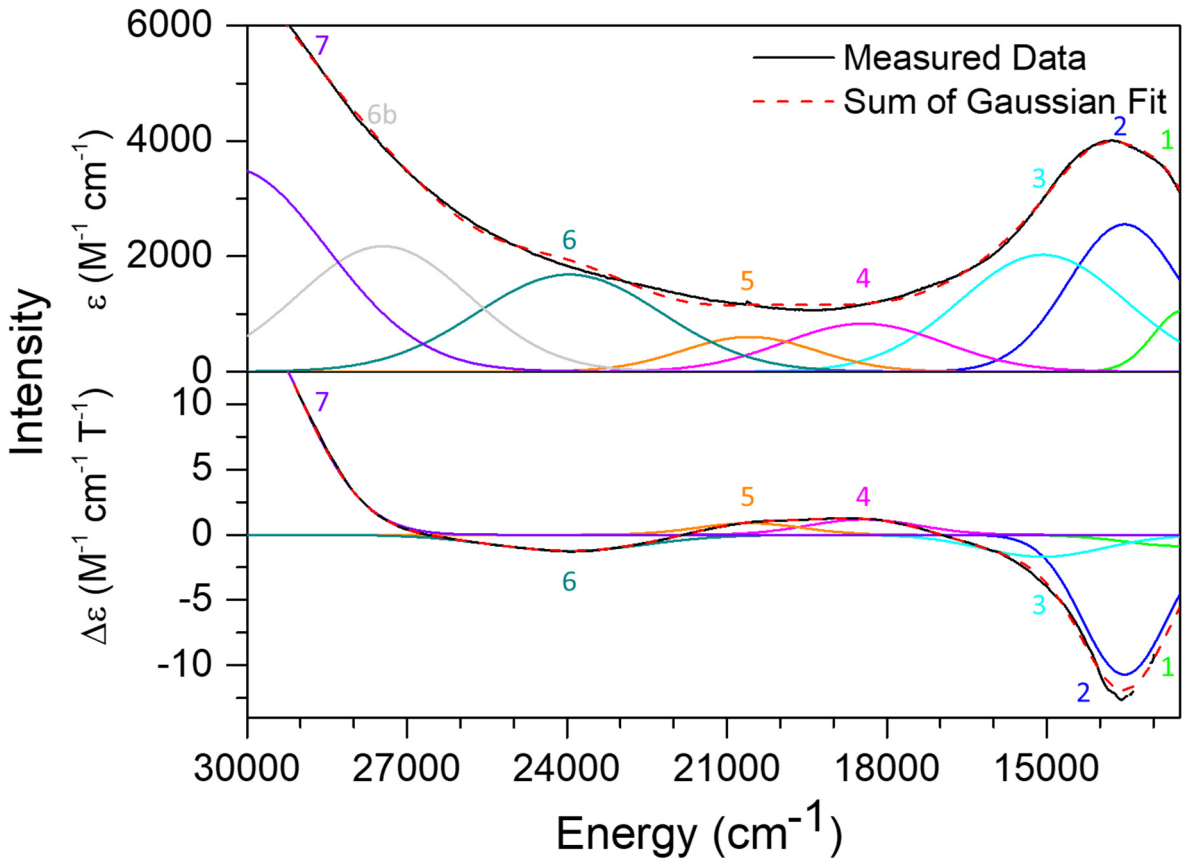

Figure 3. UV-Vis and MCD data for intermediate **3**, along with a correlated Gaussian fit of these data (see Table 1). Top: UV-Vis spectrum of **3** obtained at 0.20 mM concentration in MeCN at –40 ºC. Bottom: MCD data of **3** obtained at 3 mM concentration at 2 K 7 T, in a frozen glass prepared by reacting $Li_2[Ni^{II}(TAML)]$ (3.0 mM) with CAN (2.0 equiv.) in the presence of H_2O (5 µL) in acetonitrile/butyronitrile (1:2) at –60 ºC. Temperature and field-dependent MCD data are shown in Figures S12 and S13, respectively. Further details on the Gaussian fits of these spectra can be found in Figures S15 and S16.

From the temperature- and field-dependent MCD data of bands 2 and 7, obtained at various magnetic fields, 0 - 7 T, and various temperatures, 2 - 50 K, the magnetic saturation data shown in Figure 4 were obtained. First, since the MCD features of **3** are temperature-dependent, they correspond to **C**-term signals, which demonstrates that the complex is paramagnetic (S_t = 1 or 2). We then attempted to fit the VTVH data for both main MCD features for the S_t = 1 and 2 states. However, as shown in Figure 4, the data cannot be fit with an S_t = 2 ground state, due to the wrong curvature of the saturation curves (see Figure S17 for further S_t = 2 fitting attempts). As the spin multiplicity increases, the MCD saturation curves become more strongly curved, which is already evident from the simple Brillouin function. The analysis of our VTVH data therefore clearly demonstrates that the formally $Ni^{IV}(O)$ species **3** has an intermediate spin state, S_t = 1 (Figure 4, top). The best fit of the VTVH data was obtained using D = 4.0 cm^{-1}, E/D = 0.24, and g

= 2.013, 2.070, 2.078, which are based on DFT-predicted zero-field splitting parameters as discussed below. Note that the VTVH MCD data could be reasonably fit with a positive *D* value of up to 6 cm^{-1}, see Figure S18. This *D* value is consistent with the relatively large positive *D* value calculated for DFT structures B3LYP (2) and B3LYP (3), which are the best models for the structure of the intermediate, see Table 1 and Section 2.5. The *E*/*D* and *g* values had to be determined by calculation, as the integer spin EPR-silent species **3** prevented experimental determination of these parameters. B3LYP (2) and B3LYP (3) show good agreement for these ZFS parameters, but B3LYP (3) was ultimately chosen as it better models the Ni-OH bond length observed experimentally.

In addition, the fitting of the magnetic saturation curves also provides insight into the polarizations of the corresponding electronic transitions. Based on our fits, both bands 2 and 7 show a large degree of z-polarization, which some additional contribution from y polarization. These polarizations are relative to the orientation of the ZFS-tensor, which is accessible from DFT calculations. As one would expect, the DFT calculations show that the z direction of the ZFS-tensor is associated with the unique Ni–O axis (see Figure S19). These results indicate that bands 2 and 7 have charge transfer character between the Ni center and the oxo ligand. Further insight into the assignments of these bands is available from the TD-DFT data, as discussed below.

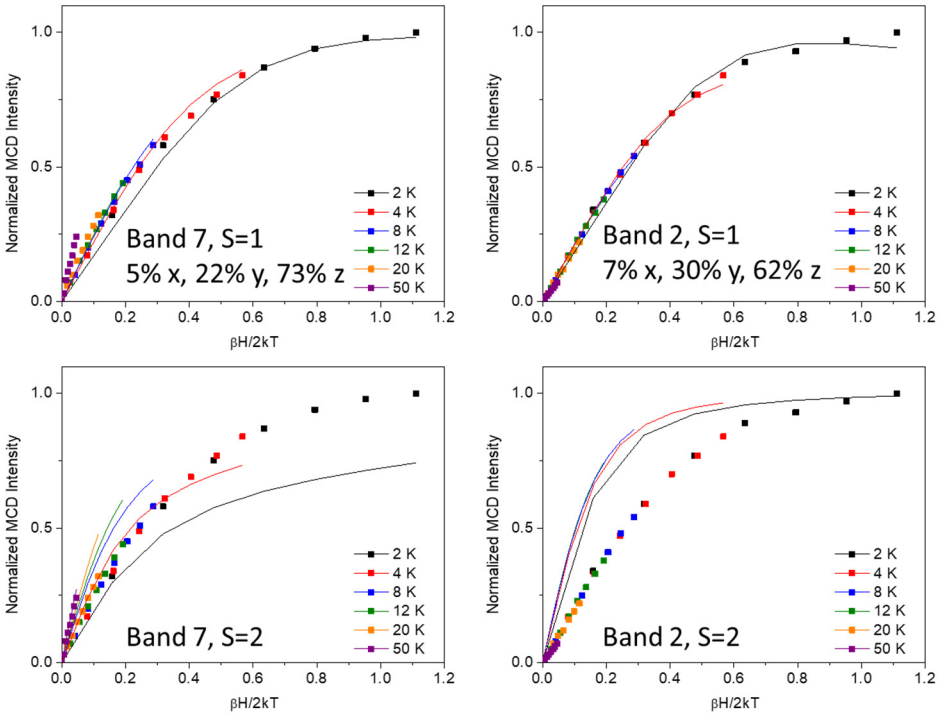

Figure 4. MCD VTVH data of **3** obtained at temperatures of 2 - 50 K and magnetic fields of 0 - 7 T, for the two main signals in the MCD spectra, bands 2 (VTVH data obtained at 14265 cm^{-1}, 701 nm, right) and 7 (VTVH data obtained at 28570 cm^{-1}, 350 nm, left). Top panels: the data fit very well with an S_t = 1 ground state, using *D* = 4.0 cm^{-1}, *E*/*D* = 0.24, and *g* = 2.013, 2.070, 2.078. Bottom panels: all attempt to fit the data with S_t = 2 failed. The dots are the experimental data while the lines correspond to the fits.

Table 1. Summary of Gaussian fitting and band assignments of the optical spectra for **3**. See Table S16 for further TD-DFT information.

No.	Energy (cm^{-1})	Intensity		Assignment	Polarization (%x, %y, %z)
		MCD Δε (M^{-1} T^{-1} cm^{-1})[a]	UV-Vis ε (M^{-1} cm^{-1})		
1	12440	-2.6	1060		-
2	13540	-26.7	2553	coligand (π∗), $O(p_y)\_d_{yz}$ (π*) → $d_{x2-y2}/d_{z2}\_O(p_z)$ (σ*), Ni-OH/O (π*) → $O(p_x)\_d_{xz}$ (π*)	7, 30, 62
3	15080	-4.3	2026		-
4	18440	3.5	831		-
5	20580	2.7	600		-
6	23960	-2.2	1682		-
6b	27450	--[b]	2175		-
7	29450	42.9	3528		5, 22, 73

[a] MCD intensity given for the 2 K 1 T spectrum, see Figure S16 for fit details.
[b] Band 6b not observed by MCD.

2.5. Density Functional Theory (DFT) Calculations.

With these experimental results in hand, we set out to model the putative high-valent Ni(O) intermediate using DFT calculations, in direct comparison to our experimental results. Based on the EXAFS analysis, which shows a short Ni–O vector and indicates that the complex is six-coordinate, we used the DFT calculations to interrogate the nature of the sixth ligand, X, and develop structural models for the intermediate. We also investigated a five-coordinate species, for comparison. As discussed above, the MCD data indicate that **3** has an S_t = 1 ground state, though we also investigated analogous S_t = 2 species, to compare structural features and total energies. For this purpose, B3LYP and other functionals were employed, in combination with the TZVP basis set. The results from our DFT calculations are summarized in Table 2, and selected structures are shown in Figure S20.

To begin, we optimized the structure of a simple, five-coordinate model, with a square-pyramidal structure where the oxo ligand occupies the apical position, in the S_t = 1 state. This structure shows a rather long Ni–O bond of 1.98 Å, which does not reproduce the experimental Ni–O distance well, especially when compared to a five-coordinate fit of the EXAFs data, which puts the Ni–O distance at 1.73 Å. Since our XAS data indicate that **3** is a six-coordinate species, we then explored structures with the sixth ligand, X, corresponding to ammonia, water, acetonitrile, and hydroxide, which are all species that are present in solution. However, in our DFT geometry optimizations (B3LYP/TZVP), the neutral ligands ammonia, water and acetonitrile all dissociated from the Ni center, which remained five-coordinate. The only six-coordinate structure that we could optimize has hydroxide coordinated in trans position to the formally oxo group. However, this structure, designated as B3LYP (1) in Table 2, has a very long Ni–O bond length of 2.15 Å, compared to the experimental Ni-O distance from the EXAFS fit for a six-coordinate complex, 1.84 Å. In this structure, the predicted Ni–OH distance is 2.27 Å. In this case, the Ni

center has the (antibonding) d_{z2} orbital singly occupied, as shown in Scheme 3, left, leading to a weakening of the axial Ni–O/OH bonds. The d_{x2-y2} orbital constitutes the LUMO in this case, as shown in Scheme 3, left. However, complex **3** can also exist in the alternative valence tautomer where instead, the (antibonding) d_{x2-y2} orbital is singly occupied and d_{z2} is empty (and constitutes the LUMO), which should lead to a strengthening of the axial Ni–O/OH bonds (Scheme 3, right). Starting our geometry optimization by locking the Ni–O distance at the experimental distance (1.84 Å), letting this structure relax into a local minimum, and then fully optimizing this structure, we are able to obtain a fully optimized structure for the alternative valence tautomer as well. This optimized structure, B3LYP (2), shows a Ni–O bond length of 1.84 Å and is only 2 kcal/mol higher in energy than B3LYP (1). However, the Ni-OH bond length predicted for B3LYP (2) is much shorter, 1.94 Å, than the experimental value of 2.22 Å. This Ni–OH bond, however, is a very soft coordinate. When the Ni–OH bond length is increased from 1.94 to 2.22 Å in a relaxed potential energy surface (rPES) scan, the calculated energy increases by only ~3 kcal/mol (Figure S21). Interestingly, as the Ni-OH distance is increased in this rPES scan, the LUMO gradually converts from the d_{x2-y2} to the d_{z2} orbital, via linear combinations of these two orbitals (Figure S22). Due to the flexibility of the Ni-OH bond, it is likely that hydrogen bonding, via the ammonia or water molecules in solution, could contribute to a longer Ni–OH bond length experimentally. Optimized structures of the relevant valence tautomer (2) with TPSSh and BP86 were also obtained, as shown in Table 2.

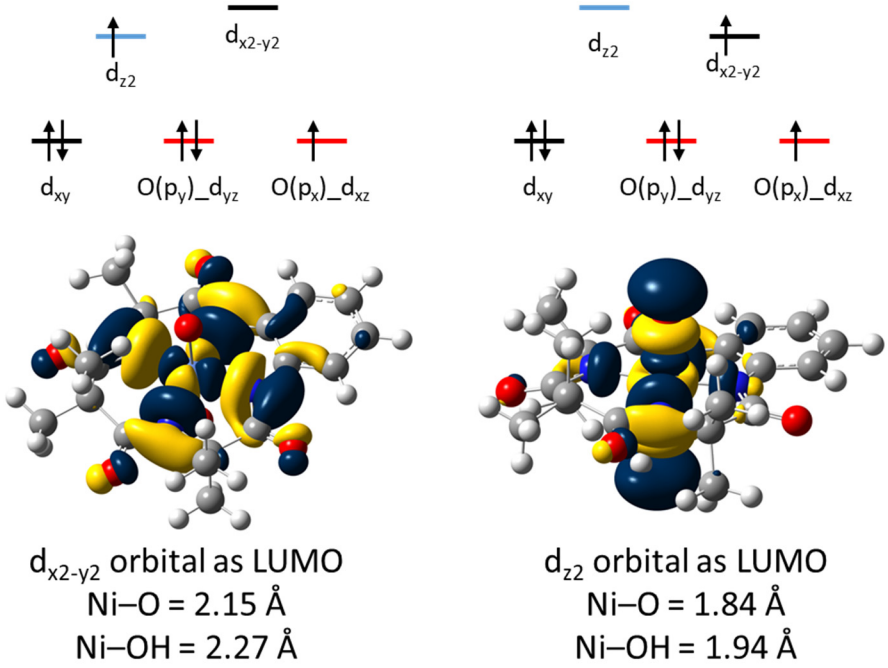

Scheme 3. Six-coordinate structures for two different valence tautomers of $[Ni(TAML)(O)(OH)]^{3-}$ were optimized for the S_t = 1 ground state, using B3LYP/TZVP. Left: the valence tautomer (1) has the d_{z2} orbital singly occupied, and the LUMO corresponds to the d_{x2-y2} orbital (contour plot shown on the bottom). Right: the valence tautomer (2) has the d_{x2-y2} orbital singly occupied, and the LUMO corresponds to the d_{z2} orbital (contour plot shown on the bottom). The calculated bond lengths are also included. The colors used in the ligand field diagrams on the top correspond to the bonding properties of these d-orbitals with respect to the oxo ligand (as in Scheme 1): blue is σ-antibonding, black non-bonding, and red π-antibonding.

Calculated ZFS parameters for both valence tautomers (S_t = 1) are also included in Table 2. While B3LYP (1) shows a negative D value around -5 cm^{-1} and moderate rhombicity, the other valence tautomer, B3LYP (2) and also B3LYP (3), shows a positive D value around 8 – 10 cm^{-1} and more pronounced rhombicity. The calculated rhombicity is somewhat surprising, given the general octahedral symmetry of the coordination environment of the Ni center, but note that the benzene ring in the coligand restricts two of the nitrogens such that there is a tight <N-Ni-N angle of 85°, while the opposing angle extends to 103°.The experimental VTVH data are best fit with D = 4.0 cm^{-1} (with E/D fixed at the calculated value of 0.24; see Figure 4 and discussion above). The calculated orientation of the ZFS-tensor for B3LYP (3) is shown in Figure S19, with the z-direction oriented along the Ni–O vector.

For comparison, we further optimized the five- and six-coordinate structures (the latter with bound hydroxide) in the S_t = 2 state, and these results are included in Table 2. Importantly, both the five- and six-coordinate S_t = 2 structures are significantly higher in energy than their S_t = 1 counterparts, by 9 and >15 kcal/mol, respectively. Taking further into consideration the results from the analysis of the VTVH MCD data (see above), it is clear that the S_t = 2 ground state can be ruled out for **3**.

In summary, while the $[Ni(TAML)(O)(OH)]^{3-}$ intermediate (**3**) could exist in two possible electronic ground states, based on the EXAFs data, the valence tautomer with the shorter Ni-O bond length, (2), is favored (with d_{x2-y2} singly occupied). The sixth ligand is modeled with hydroxide, which forms a flexible Ni–OH bond, likely modulated by hydrogen bonding. For further analysis of the electronic structure of this intermediate, we generated a third structure, B3LYP (3), where the Ni-O and Ni-OH bond distances were fixed based on the experimental (EXAFS) distances, and the rest of the structure was reoptimized (see Table 2). This model is only slightly higher in energy than both of the minimum structures, B3LYP (1) and B3LYP (2).

Table 2. DFT-calculated properties for **3**, compared for different coordination numbers, spin states, and using different functionals. All calculations were performed with the basis set TZVP. Relative energies are only compared across analogous structures, applying the same functional, and are color coded for guidance. See Figure S20 for select structures and Tables S6 – S15 for Cartesian coordinates.

			S_t = 1						S_t = 2			
			5C[a]	6C[b]					5C	6C		
		Exp. (EXAFS)	B3LYP	B3LYP (1)[c]	B3LYP (2)[d]	B3LYP (3)[e]	TPSSh	BP86	B3LYP	B3LYP	TPSSh	PBE0
	Relative Energy (kcal/mol)		0	0	2	5	0		9	18	17	
Geometry	Ni-O bond (Å)	1.84	1.98	2.15	1.84	1.84[f]	1.81	1.79	1.70	1.84	1.77	1.75
	Ni-OH bond (Å)	2.2	-	2.27	1.94	2.22[f]	1.93	1.97	-	2.26	2.28	2.20
	Avg. Ni-N bond (Å)	1.96	1.88	1.89	1.97	1.93	1.96	1.98	1.99	1.98	1.98	1.97
	Σ<N-Ni-N (°)	-	356	360	360	360	360	360	337	358	355	360
	<O-Ni-OH (°)	-	-	179	179	179	178	178	-	179	178	179
	<Ni-O-H (°)	-	-	97.3	101.1	97.6	100.4	99.1	-	98.4	95.9	98.6
	[C18-Ni-O-H (°)[g]	-	-	-0.1	-20.6	0.4	-8.0	-15.0	-	-8.5	-0.1	-0.1
Vibration	Ni-O (cm^{-1})	-	385 (393)	258, 262, 270	507	N/A	540	585	734	392 (375,363)	585	613, 615
	Ni-OH (cm^{-1})	-	-	202, 213	439	N/A	451, 457	399	-	169, 175, 225, 229	133, 160, 227, 281	184, 242, 292
Spin Density	Ni	-	0.65	0.64	0.75	0.73	0.78	0.83	1.82	1.85	1.82	1.81
	O	-	1.31	1.18	0.95	1.07	0.9	0.74	1.28	1.32	1.30	1.40
	OH	-	-	0.15	-0.06	0.03	-0.05	-0.01	-	0.21	0.23	0.19
	Ns (coligand)	-	0.04	0.04	0.34	0.19	0.36	0.39	0.80	0.61	0.64	0.63
	coligand (except Ns)	-	0	-0.02	0.01	-0.02	0.01	0.04	0.10	0.01	0.01	-0.03
EPR	*D*	-	NC[h]	-4.76	8.93	10.47	NC	NC	-1.03	-113	NC	NC
	E/*D*	-	NC	0.11	0.30	0.24	NC	NC	0.11	0.10	NC	NC

[a] 5C: five-coordinate structure. [b] 6C: six-coordinate structure. [c] B3LYP (1) is the fully optimized, minimum energy six-coordinate structure for S_t = 1, with d_{z2} singly occupied. [d] B3LYP (2) is the fully optimized, six-coordinate structure for S_t = 1, with d_{x2-y2} singly occupied (which constitutes a local minimum). [e] B3LYP (3) is a partially optimized structure with the Ni–O and Ni–OH bonds locked at the experimental (EXAFS) distances. [f] These bond distances were fixed during the optimization of structure B3LYP (3). [g] C18 is the dimethylated carbon between the two carbonyls of the amide groups in the $TAML^{4-}$ ligand. [h] NC: not calculated.

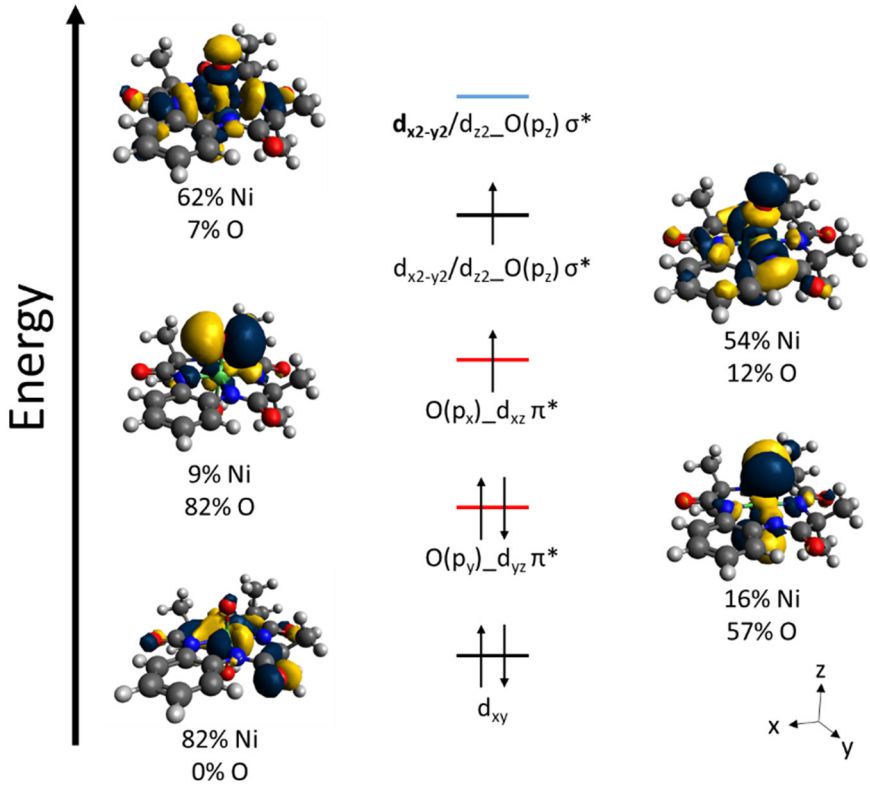

Scheme 4. MO diagram of $[Ni(O)(OH)(TAML)]^{3-}$. These molecular orbitals were calculated using TPSSh/TZVP for the B3LYP (3) optimized structure and visualized in Avogadro. Shown are the corresponding β-spin MOs.

To further interrogate the electronic structure of the $[Ni(TAML)(O)(OH)]^{3-}$ intermediate (**3**), we then analyzed the MO diagram for the B3LYP (3)-optimized structure, using TPSSh/TZVP calculations. As shown in Scheme 4, with the Ni-OH bond set to 2.22 Å, the $d_{x^2-y^2}$ and d_{z^2} orbitals become somewhat mixed, making it difficult to assess the strength of the Ni–O σ bond. This information is more readily available from the MO diagram of the B3LYP (2) structure with the shorter Ni–OH bond. In this case, the LUMO of the complex is the antibonding combination of d_{z^2} and the $O(p_z)$ orbital, $d_{z^2}\_O(p_z)$, which has 54% Ni(d) and 16% O character, as shown in in Figure S23. The corresponding bonding MO at lower energy is fully occupied, giving rise to a Ni–O σ bond with a formal bond order of 1. To lower energy, the first SOMO is the $d_{x^2-y^2}$ orbital, which is non-bonding to the oxo ligand. As shown in Scheme 4, the two dπ orbitals of Ni, d_{xz} and d_{yz}, undergo π-bonding interactions with the $O(p_x)$ and $O(p_y)$ orbitals. Here, both π-bonding interactions are inverted, with the antibonding combinations shown in Scheme 4 having dominant O(p) character. However, in the case of d_{yz}, both the bonding combination with $O(p_y)$ at lower energy and the antibonding combination at higher energy, shown in Scheme 4, are fully occupied, which means that this orbital interaction does not contribute to the Ni–O bond. In the case of d_{xz}, the bonding combination with $O(p_x)$ at lower energy is doubly occupied, but the corresponding

antibonding MO is only singly occupied, as shown in Scheme 4, which means that this orbital interaction could contribute 1/2 bond order to the Ni–O bond. However, as shown in Scheme 4, the orbital $O(p_x)\_d_{xz}$ shows very strong bond inversion, with 82% O(p) and only 9% Ni(d) contribution. Hence, this interaction constitutes a very weak Ni–O π-bond, which means that the Ni–O bond in **3** is de facto a Ni–O single (σ) bond. In addition, the oxo ligand in **3** is oxidized and has very clear oxyl character, as reflected by its large amount of spin density of about +1.0, creating a "hole" in the $O(p_x)$ orbital (see Figure S24 for a larger image of the electron hole). Therefore, the electronic structure of **3** is best described as a Ni(III)-$O^{\bullet-}$ complex, where the spins of the Ni(III) (S = 1/2) and the oxyl ligand (S = 1/2) are ferromagnetically coupled (see spin densities listed in Table 2), giving the experimentally observed S_t = 1 ground state. In other words, the oxo ligand serves as a non-innocent ligand in **3**. In contrast, and surprisingly, the $TAML^{4-}$ ligand is not redox-active in complex **3**, and does not accumulate any notable spin density. This is surprising, considering that large number of M(IV)-$TAML^{4-}$ complexes have been reported where the TAML ligand is bound in the one-electron oxidized, $TAML^{\bullet 3-}$, form.[1,48–50] The Ni(III)-$O^{\bullet-}$ electronic structure description of **3** as outlined above implies that the Ni–O bond is actually quite weak. In agreement with this finding, the calculated Ni–O stretching frequency is located around 500 cm^{-1}, as shown in Table 2, which reflects the single bond character of the Ni–O interaction. Finally, as expected, the nonbonding d_{xy} orbital is lowest in energy and has no contribution from the oxyl ligand.

To further assign the optical spectra of **3**, we performed TD-DFT calculations, using the B3LYP (3) structure and the functionals B3LYP, TPSSh, BP86, and PBE0, which contain varying amounts of Hartree-Fock exchange. Figure 5 compares the absorption spectra calculated with these functionals to the experimental data. As evident from the figure, TPSSh matches the experimental absorption spectrum the best. TD-DFT predicts a broad absorption band around 550 nm (18000 cm^{-1}), which corresponds to the calculated transitions 6 – 13 and which we assign to the experimental absorption band at 728 nm (13740 cm^{-1}) that is indicative of the formation of **3**. Through TD-DFT, we found that this spectral region is mostly dominated by mixed ligand-to-metal charge transfer (CT) transitions, mostly into $d_{x2\text{-}y2}/d_{z2}\_O(p_z)$ (σ^*) as the acceptor MO, in agreement with the mixed polarizations observed for band 2 (see Figure 3 and Table 1). Interestingly, we do not see much CT into the $O(p_x)\_d_{xz}$ hole in the low-energy region of the absorption spectrum. Of the TD-DFT predicted excitations, transition 10 is the only one with significant z polarization (88%), corresponding to a coligand (π) → $d_{x2\text{-}y2}/d_{z2}\_O(p_z)$ (σ^*) and Ni-OH/O (π^*) → $O(p_x)\_d_{xz}$ (π^*) transition.

In the visible range of the spectrum (experimental bands 4 - 6), TD-DFT predicts mostly CT transitions originating from aryl/amide(π) and amide-O lone pairs into the $d_{x2\text{-}y2}/d_{z2}\_O(p_z)$ (σ^*) and $O(p_x)\_d_{xz}$ orbitals of the Ni–O unit, none of which have much oscillator strength (calculated bands 18 to 39; see Table S16). Finally, a number of calculated bands (44 – 58) with larger oscillator strengths are found in the energy region of band 7. However, these features are mostly intra-coligand π → π^* transitions, with some admixture of Ni-O ($\pi*$) → aryl/amide (π^*) and amide-O lone pair → $d_{x2\text{-}y2}/d_{z2}\_O(p_z)$ (σ^*) and $O(p_x)\_d_{xz}$ CT character, with anywhere between 5 – 25% z polarization. Further information on the TD-DFT results and assignments can be found in Table S16.

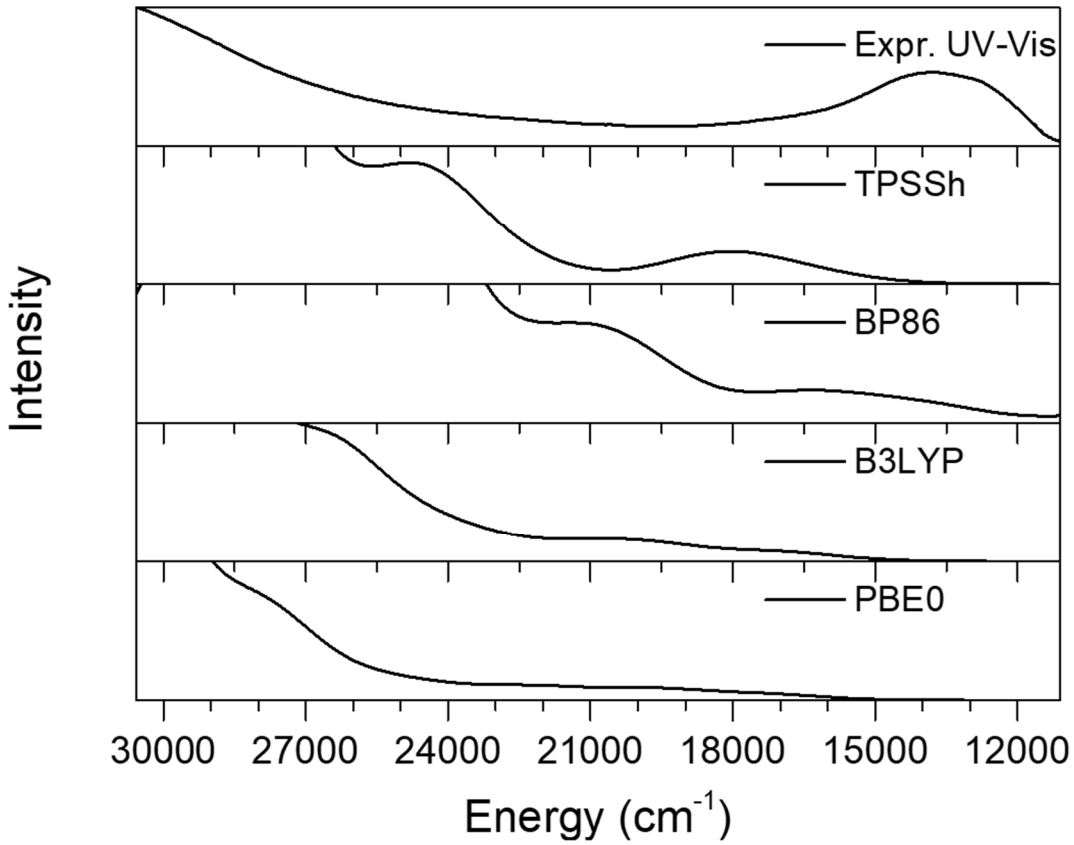

Figure 5. TD-DFT calculations on structure B3LYP (3), where the Ni–O and Ni–OH bond lengths were fixed at the experimental values (from EXAFS; see Table 2 and text). All TD-DFT calculations were performed with the program ORCA, using the indicated functionals and the TZVP basis set.

We also performed TD-DFT calculations for the other structures, B3LYP (1) and B3LYP (2), and these results are shown in Figure S25. It is notable here that the TD-DFT calculations for valence tautomer B3LYP (1) with the long Ni–O bond (d_{z2} orbital singly occupied) show by far the worst agreement with the experimental absorption spectrum, further indicating that this is not the experimentally observed valence tautomer. Comparing the TD-DFT results for structures B3LYP (2) with the short Ni–O bond (d_{x2-y2} orbital singly occupied) and the analogous B3LYP (3) with the longer Ni–OH bond, it is notable that B3LYP (3) with the weakly coordinated sixth ligand does in fact reproduce the experimental absorption spectrum the best, in support of the EXAFS results.

2.6. Reactivity Studies of 3.

We investigated the reactivity of **3** in oxygen atom transfer (OAT) and hydrogen atom transfer (HAT) reactions.

(i) OAT Reaction by 3. First, the reactivity of **3** was investigated with thioanisole derivatives. Upon addition of thioanisole to a solution of **3** in MeCN at –40 °C, **3** disappeared at a very fast rate. Therefore, a stopped-flow UV-Vis spectrophotometer was used to determine the reaction rate. The reaction obeyed the first-order kinetics, and the rate constant increased linearly

with increasing the thioanisole concentration to give a second-order rate constant (k_2) of 4.3 × 10^3 M^{-1} s^{-1} at –40 °C (Table S17). Reactions of **3** with thioanisole derivatives bearing an electron-donating substituent (4-MeO-thioanisoles and 4-Me-thioanisoles) were too fast to follow even at −40 °C using stopped-flow UV-Vis spectroscopy. Hence, electron-withdrawing *para*-substituted thioanisoles were used to determine reaction rates. The second-order rate constants (k_2) of 4-X-substituted thioanisoles (X = NO_2, CN, Br, and Cl) were determined in MeCN at –40 °C (Table S17 and Figures S26 and S27). When the logarithm of the second-order rate constants (log k_2) is plotted against the one-electron oxidation potentials (E_{ox}) of 4-X-substituted thioanisoles, a large negative slope of –12 is obtained (Figure 6. ***Plots*** of log k2 *against* (a) the Eox *values* and (b) the σp+ *values* of 4-X-substituted thioanisoles (X = NO2, CN, Br, Cl, and H) in the reactions of 3 **and** thioanisole derivatives in MeCN at −40 °C. (Figure 6a) indicate that the OAT reaction occurs via an electron-transfer mechanism. In addition, when the logarithm of the second-order rate constants (log k_2) is plotted against σ_p^+ values of 4-X substituted thioanisole derivatives, a large negative ρ value of –5.3 is obtained in the Hammett plot (Figure 6b), indicating an electrophilic nature of **3**. Product analysis of the thioanisole oxidation reactions revealed the formation of methyl phenyl sulfoxide as an organic product. In addition, the thioanisole oxidation reaction carried out with **3**-^{18}O revealed the 85% ^{18}O incorporation into the methyl phenyl sulfoxide (Figure S28). The main inorganic product, characterized by CSI-MS and EPR spectroscopy, was $[Ni^{III}(TAML)]^-$ (Figure S29). Thus, the results of the product analysis led us to propose that the reaction of **3** and thioanisole afforded the methyl phenyl sulfoxide and $[Ni^{II}(TAML)]^{2-}$ products and the $[Ni^{II}(TAML)]^{2-}$ product reacted with **3** to give $[Ni^{III}(TAML)]^-$ via a comproportionation reaction (Figure S10).

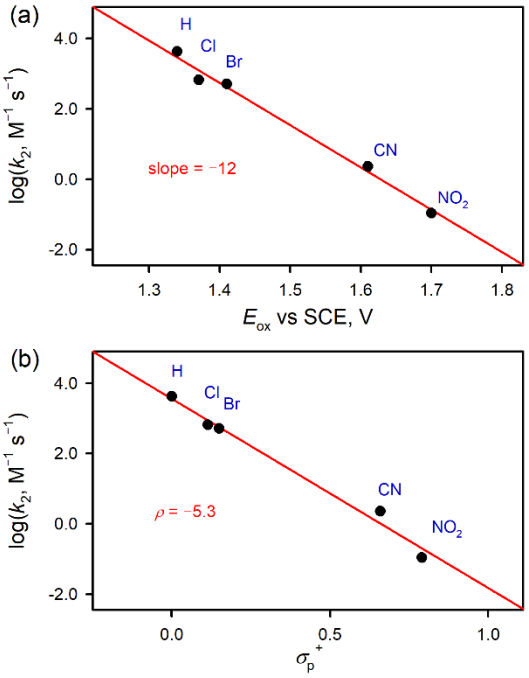

Figure 6. Plots of log k_2 against (a) the E_{ox} values and (b) the σ_p^+ values of 4-X-substituted thioanisoles (X = NO_2, CN, Br, Cl, and H) in the reactions of **3** and thioanisole derivatives in MeCN at −40 °C.

Next, styrene derivatives were used to investigate the reactivity of **3** in the OAT reaction. A second-order rate constant (k_2) of 2.5 M^{-1} s^{-1} was determined in the oxidation of styrene by **3**

in MeCN at –40 °C (Table S18 and Figure S30). Similarly, second-order rate constants (k_2) of X-substituted styrenes (X= 4-Me, α-Me, 3-Me, and 4-Cl) were determined in MeCN at –40 °C (Table S18 and Figure S31). When the logarithm of the second-order rate constants (log k_2) is plotted against the one-electron oxidation potentials (E_{ox}) of X-substituted styrenes, a large negative slope of –9.6 is obtained (Figure S32a). This result indicates that the oxidation of styrene derivatives by **3** occurs via an electron transfer mechanism. Also, a large negative ρ value of –6.5 was obtained in the Hammett plot (Figure S32b), indicating again the electrophilic nature of **3**. Product analysis of the reaction solution of the styrene oxidation by **3** revealed the formation of benzaldehyde as a major organic product and $[Ni^{III}(TAML)]^-$ as an inorganic product (Figure S33).

(ii) HAT Reaction by 3. A reactivity study of **3** was performed in C-H bond activation of hydrocarbons with the bond dissociation energies (BDEs) of 75 – 82 kcal mol^{-1}, such as xanthene (75.5 kcal mol^{-1}), 1,4-cyclohexadiene (CHD, 78 kcal mol^{-1}), fluorene (80 kcal mol^{-1}), and diphenylmethane (DPM, 82 kcal mol^{-1}).[51] Addition of xanthene to a MeCN solution of **3** at 0 °C resulted in the decay of **3** (Figure 7a). The observed first-order rate constant increased with an increase in the xanthene concentration, affording a second-order rate constant (k_2) of 1.2 M^{-1} s^{-1} at 0 °C (Figure 7b). The kinetic isotope effect (KIE) for the xanthene oxidation was determined to be 7.0(3) (Figure 7b). The second-order rate constants for the reactions of CHD, fluorene, and DPM were also obtained (Table S19 and Figure S34). A plot of log k_2' versus C-H BDEs of the substrates shows a good linear correlation (Figure S35). Product analysis of the reaction solution of the oxidation of xanthene by **3**-^{18}O revealed the formation of xanthone (with 72% ^{18}O incorporation) as a major organic product (Figure S36) and $[Ni^{III}(TAML)]^-$ as an inorganic product (Figure S37).

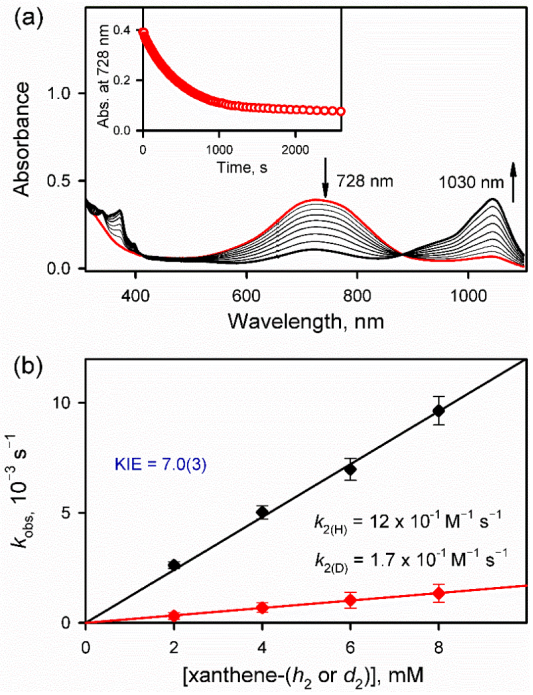

Figure 7. (a) UV-Vis spectral changes observed in the reaction of **3** (0.10 mM) and xanthene (2.0 mM) in MeCN at 0 °C. Inset shows a time trace monitored at 728 nm due to the disappearance of **3**. (b) Plot of the pseudo-first-order rate constants (k_{obs}) against the concentrations of xanthene-

h_2 (blank circles) and xanthene-d_2 (red circles) for the reactions of **3** with xanthene and xanthene-d_2 in MeCN at 0 °C.

3. Discussion

In this paper, we present the preparation and rigorous spectroscopic and theoretical characterization of a terminal Ni-oxyl complex, $[Ni(TAML)(O)(OH)]^{3-}$ (**3**). This reactive intermediate, formally a Ni(IV)-oxo complex, is generated by the oxidation of the corresponding four-coordinate Ni(II)- and Ni(III)-$TAML^{4-}$ precursors, using either CAN or an O-atom transfer agent like PhIO, at low temperature. Generation of **3** is accompanied by the rise of a new absorption feature at 728 nm in the UV-Vis spectrum. The presence of an oxo-type ligand in **3** is supported by CSI-MS spectroscopy in conjecture with ^{18}O isotope labeling. In agreement with the formal Ni(IV) state, the complex is EPR silent. For example, upon addition of 1 equiv. of CAN to a solution of the EPR-active Ni(III) precursor (S_t = 1/2), the EPR signal of this species disappears, but can be regenerated when 1 equiv. of reductant is subsequently added. These results demonstrate that complex **3** is a one-electron oxidized species compared to the Ni(III) precursor. But what is the actual nature of this species? Based on these data, it is tempting to assign **3** as a Ni(IV) complex. However, there is a reason that Ni(IV) complexes are sparse, and reports of well-characterized Ni(IV) complexes in the literature are lacking. Considering the presence of the non-innocent $TAML^{4-}$ ligand in **3**, it is clear that a thorough spectroscopic characterization is needed to order to make any claims about a high oxidation state of the Ni center in **3**.

From XAS, complex **3** shows a Ni K-edge that has an edge-energy that is essentially identical with that of the Ni(III) precursor complex, indicating that the oxidation state of the Ni center in **3** is better described as Ni(III). EXAFS shows a Ni–O vector at 1.84 Å, again confirming the presence of an oxo-type ligand, but also the presence of a sixth scatterer at about 2.2 Å from the Ni center although the nature of which cannot be identified from those data. Since **3** is EPR silent, we used low-temperature MCD spectroscopy to further delineate the optical and magnetic properties of **3**. Analysis of the VTVH MCD data of the 728 nm feature clearly shows that the intermediate has an S_t = 1 ground state with a $[d_{xy},O(p_y)\_d_{yz},O(p_x)\_d_{xz}]^5[d_{x2-y2},d_{z2}]^1$ electron configuration. The 728 nm absorption feature is deconvoluted into three transitions, which, based on the TD-DFT results, corresponds to mixed ligand-to-metal charge transfer (CT) transitions, mostly into $d_{x2-y2}/d_{z2}\_O(p_z)$ (σ^*) as the acceptor MO, in agreement with the mixed polarizations observed for band 2. This indicates the coligand oxidation and reduction of the Ni-O unit in the excited state. It is notable that this absorption feature has a quite substantial intensity in the absorption spectrum (ε = 2500 $M^{-1}cm^{-1}$), but that laser excitation of this band does not lead to the resonance enhancement of the Ni-O stretch. The complex shows a relatively small *D* value of about 4 cm^{-1} and a moderate rhombicity arising from the lack of the four-fold symmetry of the $TAML^{4-}$ ligand.

In order to obtain further insight into the nature of **3**, we then turned to DFT calculations. Structure optimizations with neutral molecules like water, solvent (CH_3CN), ammonia, etc. as the sixth ligand led to five-coordinate structural models for **3**, where the sixth ligand is expelled. However, an anionic ligand like hydroxide is able to stably coordinate to the Ni center, generating a six-coordinate structure in agreement with the EXAFS results. We therefore propose that **3** corresponds to the complex $[Ni(TAML)(O)(OH)]^{3-}$. This complex could in theory exist in either the

S_t = 1 or 2 state, but the DFT calculations show that the S_t = 2 state is >15 kcal/mol higher in energy, in agreement with the MCD result that shows an S_t = 1 ground state for **3**. DFT calculations further show that in the S_t = 1 state with a $[d_{xy},O(p_y)\_d_{yz},O(p_x)\_d_{xz}]^5[d_{x2\text{-}y2},d_{z2}]^1$ electron configuration, the d_{z2} and $d_{x2\text{-}y2}$ orbitals are quasi degenerate, which means that the complex can exist in two valence tautomers where either the d_{z2} or the $d_{x2\text{-}y2}$ orbital is singly occupied. We were able to generate optimized structures for both valence tautomers, and show that they are within 2 kcal/mol (B3LYP). However, the two valence tautomers lead to very different geometric structures for **3**, where single occupation of d_{z2} (isomer B3LYP (1) in Table 2, with the z axis along the Ni–O vector) causes a substantial increase in the Ni–O bond to 2.15 Å, in stark contrast to the experimental data. On the other hand, the valence tautomer, in which $d_{x2\text{-}y2}$ is singly occupied (isomer B3LYP (2) in Table 2), reproduces the experimental Ni–O distance of 1.84 Å exactly. Based on these results, complex **3** has the electron configuration $[d_{xy}^2,d_{yz}^2,d_{xz}^1,d_{x2\text{-}y2}^1]$ (in the coordinate system applied here), which should give rise to a strong Ni–O bond with a formal bond order of 1.5 (see Scheme 1), which is somewhat at odds with the experimental Ni–O distance of 1.84 Å.

Further analysis of the electronic structure of $[Ni(TAML)(O)(OH)]^{3-}$ shows that the Ni–O π-bond shows an unprecedented amount of bond inversion, where the antibonding combination of $O(p_x)$ and d_{xz} is largely located on the oxo ligand (82% O(p) character according to the TPSSh calculation). Therefore, the electronic structure of **3** is best described as a low-spin Ni(III) complex (S = 1/2) with a bound oxyl ($O^{\bullet-}$) ligand (S = 1/2) where the spins of the Ni and the oxyl are ferromagnetically coupled, giving rise to the observed S_t = 1 ground state for **3**. In other words, the oxo group serves as a non-innocent ligand in **3**, in agreement with the XAS results that show that the Ni center in **3** is best described as Ni(III). With this large degree of bond inversion, the Ni–O interaction is best described as a single σ-bond, in line with the observed Ni–O distance of 1.84 Å. In contrast, and surprisingly, the $TAML^{4-}$ ligand is innocent, and simply serves as a strongly donating ligand, further stabilizing the Ni–O unit in **3**. These results were further corroborated using post HF computations. NEVPT2 calculations of **3** show the compound possesses little multiconfigurational character with the leading Ni(III)-$O^{\bullet-}$ configuration comprising over 99% of the CASSCF wavefunction. Thus, the compound is best described as possessing a Ni(III)-oxyl moiety coordinated by a redox innocent $TAML^{4-}$ ligand framework.

The fact that **3** contains a Ni(III)-$O^{\bullet-}$ unit, and not a Ni(IV) center, is again in agreement with the notion that the Ni(IV) oxidation state is difficult to stabilize in complexes with organic coligands that contain N- and O-donor groups, due to the strongly oxidizing nature of Ni(IV). Correspondingly, claims of Ni(IV) complexes in the literature have to be taken with some skepticism. For example, in a recent study, the preparation of a Ni(IV)-nitrato complex was claimed.[52] Although the authors note an ~0.7 eV blue-shift of Ni K-edge XAS features of this complex relative to the Ni(III) starting material, they also acknowledge the difficulties of making oxidation state assignments on the basis of XANES edge-shifts alone. Furthermore, the authors highlight that both formal Ni(III) and Ni(IV) complexes possess significant ligand non-innocence. Therefore, the authors note that the putative Ni(IV)-nitrato complex can actually be described as a physical d^8 Ni(II) species. In other cases, the difficulty of stabilizing Ni(IV) has also been acknowledged in the literature, for example for complexes $[Ni^{III}(L)(O^{\bullet})]$ and $[Ni^{III}(dpaq)(O^{\bullet})]^+$ (see Scheme 2),[33,34] which the authors cautiously describe as Ni(III)-oxyl species (despite the fact that insufficient characterization of these complexes is available to fully support this claim, see discussion in Introduction). In addition, bond inversion is a known problem for Ni complexes, and

has even been invoked for explaining the photochemistry of Ni^{II}-aryl complexes, where a photochemically accessible ligand-field excited state induces inversion of the Ni(II)-C bond, leading to C-H activation of a THF solvent molecule.[53] Based on these considerations, $[Ni(TAML)(O)(OH)]^{3-}$ is, in fact, the first well-characterized, terminal Ni–O complex reported to this date. The quest for a true Ni(IV)-oxo complex continues.

4. Experimental Section

Materials. All chemicals, obtained from Aldrich Chemical Co. and Tokyo Chemical Industry, were the best available purity and used without further purification unless otherwise indicated. Cerium(IV) ammonium nitrate, $Ni^{II}(acac)_2$ and other substrates such as xanthene, 1,4-cyclohexadiene, fluorene, triphenylmethane, thioanisole derivatives, styrene derivatives were purchased from Aldrich Chemical Co. and used as received. Trifluromethanesulfonic acid was purchased from Tokyo Chemical Industry. $H_2{}^{18}O$ (95% ^{18}O-enriched) was purchased from Berry & Associates/ICON Isotopes (Dexter, MI, USA). Iodosylbenzene (PhIO) was prepared by the literature method.[54] $PhI^{18}O$ prepared by mixing PhIO (in 50 µL trifluroethanol) and 5 µL of $H_2{}^{18}O$ at 25 °C and using it after 20 minutes. The deuterated xanthene-d_2 was synthesized by a literature method.[55] Purity of >99% deuteration was confirmed by ^1H NMR. The H_4-TAML ($TAML^{4-}$ = tetraamido marcrocyclic ligand, 3,4,8,9-tetrahydro-3,3,6,6,9-hexamethyl-1*H*-1,4,8,11-benzotetraazocyclotridecane-2,5,7,10-(6*H*,11*H*)-tetrone) was purchased from GreenOx Catalyst, Inc. (Pittsburgh, PA, USA) and used as received. The $Li_2[Ni^{II}(TAML)]$ complex was synthesized by reaction of deprotonated $TAML^{4-}$ ligand with $Ni^{II}(acac)_2$ under inert atmosphere in dry and deoxygenated tetrahydrofuran (THF).

Instrumentation. UV-Vis spectra were recorded on a Hewlett Packard Agilent 8453 UV-Vis spectrophotometer equipped with an UNISOKU USP-203 cryostat system and a UNISOKU RSP-601 stopped-flow spectrometer equipped with a MOS-type highly sensitive photodiode array detector with an UNISOKU USP-204-09 cryostat system (UNISOKU, Japan), or on a Hi-Tech Scientific SF-61 DX2 cryogenic stopped-flow spectrometer equipped with a Xe arc lamp and a KinetaScan diode array rapid scanning unit (TgK Scientific, U.K.). The cold-spray ionization time-of-flight mass (CSI-TOF-MS) spectral data were collected on a JMS-T100CS (JEOL, Japan) mass spectrometer equipped with the CSI source [conditions: needle voltage = 2.2 kV, orifice 1 current = 50–500 nA, orifice 1 voltage = 0–20 V, ring lens voltage = 10 V, ion source temperature = 5 °C, spray temperature = −40 °C]. CSI-MS spectra of Ni complexes were obtained by infusing the reaction solution directly into the ion source through a pre-cooled tube under high N_2 gas pressure. X-band CW-EPR spectra were recorded at 5 K using X-band Bruker EMX-plus spectrometer equipped with a dual mode cavity (ER 4116DM). Low temperature was achieved and controlled with an Oxford Instruments ESR900 liquid He quartz cryostat with an Oxford Instruments ITC503 temperature and gas flow controller. The experimental parameters for EPR measurements were as follows: Microwave frequency = 9.647 GHz, microwave power = 1.0 mW, modulation amplitude = 10 G, gain = 1×10^4, and modulation frequency = 100 kHz. EPR spectra were also recorded at 77 K with use of JEOL X-band spectrometer (JES-FA100). The *g* value was calibrated using the Mn^{2+} marker. The EPR spectra were recorded under non-saturating microwave power conditions. The magnitude of modulation was chosen to optimize the resolution and the signal-to-noise (S/N) ratio of the observed spectra. The experimental parameters for EPR measurements by JES-FA100 were as follows: microwave frequency = 9.007 GHz, microwave

power = 1.0 mW, modulation amplitude = 3.0 G, modulation frequency = 100 kHz and time constant = 0.03 s. Product analysis was performed using an Agilent Technologies 6890N gas chromatograph (GC), and an ISQ 7000 (single quadrupole) mass spectrometer (Thermo Scientific, Austin, Texas, USA) interfaced with TRACE 1310 gas chromatograph (GC-MS), or high performance liquid chromatography (HPLC, Waters 515) equipped with a Waters 2998 Photodiode array detector. Product analysis was performed using high performance liquid chromatography (HPLC, Waters 515) on Hypersil GOLD column (5 µm, 4.6 × 250 mm), and product yields were determined with a UV Detector at 215 and 254 nm. Cyclic voltammetry (CV) measurements were performed on a CHI630B electrochemical analyzer (CH Instruments, Inc.) under an Ar atmosphere in a deaerated mixture of MeCN/H_2O (v/v 19:1) containing 0.10 M $^nBu_4NPF_6$ ($TBAPF_6$) as the supporting electrolyte at -40 °C. A conventional three-electrode cell was used with a platinum working electrode (surface area of 0.30 mm^2), a platinum wire used as a counter electrode and an Ag/$AgNO_3$ (0.010 M) electrode as a reference electrode. The measured potentials were recorded with respect to an Ag/Ag^+ reference electrode. All potentials (vs Ag/Ag^+) were converted to values vs SCE by adding 0.29 V.

The MCD spectroscopy setup uses an Oxford SM4000 cryostat and a JASCO J-815 CD spectrometer. The SM4000 cryostat uses a liquid helium-cooled super conducting magnet, providing magnetic fields of 0-7 T. A gaseous nitrogen-cooled xenon lamp is the light source for the JASCO J-815 CD spectrometer, and the detector is a photomultiplier in the UV-Vis range. The samples are loaded into the Oxford Cryostat variable temperature insert (VTI) chamber, which can reach temperatures 1.5 K – 300 K and has four optical windows made of Suprasil B quartz for optical access to the sample. The temperature was set to 2, 4, 8, 12, 20, and 50 K in sequence and spectra were recorded between 300 and 900 nm at varying fields (-7 to +7 T) for each temperature. The UV-Vis and MCD data were fit using the program PeakFit (v. 4.12) using the fewest Gaussians required, with the quality of fit evaluated by X^2.

Electronic Structure Calculations. Geometry optimization and frequency calculations were performed using Gaussian 09.[56] The functionals B3LYP,[57–59] BP86,[57,60] PBE0,[61] and TPSSh[62–64] were used with the basis set TZVP for all of these calculations. ORCA (version 4.0)[65] was used to perform the EPR and time-dependent DFT calculations on the corresponding, optimized structures. Ni K-edge TD-DFT calculations were performed using ORCA (version 5.0.3) on all optimized structures from above using the B3LYP hybrid density functional, the ZORA relativistic approximation, and employing the ZORA-def2-TZVP(-f) basis set and SARC/J auxiliary basis set on all atoms. The first 25 roots were calculated. The resulting calculated transitions were blue-shifted 247.1 eV. A Gaussian was applied to each transition (1.2 eV peak width) and summed.

Synthesis of $[Ni^{II}(TAML)]^{2-}$ (1). The $Li_2[Ni^{II}(TAML)]$ was synthesized by deprotonating H_4-TAML (200 mg) ligand with lithium bis(trimethylsilyl)amide (3.0 mL of 1.0 M THF solution) under argon atmosphere in dry and deoxygenated tetrahydrofuran (THF) (30 mL) at 25 °C, followed by slow addition of $Ni(acac)_2$ (210 mg) dissolved in 2 mL CH_3CN. The reaction mixture was stirred overnight and then the solvent was removed on the rotary evaporator, giving dark yellow solid. The solid was dissolved in minimum amount of H_2O and filtered, and the filtrate was evaporated to dryness under reduced pressure, leaving yellow solid of $Li_2[Ni^{II}(TAML)]$. The complex was further purified using water-acetonitrile mixture. $Li_2[Ni^{II}(TAML)]$ is highly soluble in water but have poor solubility in organic solvents. Hence for all reactions, 5.0 µL of H_2O was used to dissolve **1** which was then added to 2 mL of acetonitrile. To improve solubility of **1** for crystallization, counter-ion Li^+ was exchanged with $(K(2.2.2\text{-cryptand}))^+$. $(K(2.2.2\text{-cryptand}))_2[Ni^{II}(TAML)]$ complex was

synthesized by stirring the solution of $Li_2[Ni^{II}(TAML)]$ with KCl (excess) and 2,2,2-cryptand (5 equiv) in water. The obtained solid was filtered, washed with water, dried and recrystallized in acetonitrile/Et_2O solution. Yellow crystals suitable were successfully grown by storing a solution of $[Ni^{II}(TAML)]^{2-}$ in acetonitrile/diethyl ether (1:10) at 25 °C.

Generation and isolation of $[Ni^{III}(TAML)]^-$ (2). $Li[Ni^{III}(TAML)]$ was generated by oxidizing $Li_2[Ni^{II}(TAML)]$ with 1 equiv of CAN in MeCN at 25 °C. **2** is highly stable at room temperature and it does not show reactivity with substrates such as thioanisole, styrene or xanthene. Solid powder was isolated by adding diethyl ether directly into an MeCN solution of $Li[Ni^{III}(TAML)]$. For crystallization of **2**, cation exchange from Li^+ ion to PPh_4^+ ion was performed by adding 10 equiv of PPh_4Cl to a solution of $Li[Ni^{III}(TAML)]$ in MeCN. Single crystals of $PPh_4[Ni^{III}(TAML)]$ were obtained by slow diffusion of Et_2O into a saturated MeCN solution of $PPh_4[Ni^{III}(TAML)]$ at −20 °C.

Generation of $[Ni^{IV}(O)(OH)(TAML)]^{3-}$ (3). **3** was generated by reacting **1** (0.20 mM) with CAN (0.40 mM) in the presence of H_2O (5.0 µL) in MeCN at −40 °C. Alternatively, **3** can also be generated by reacting **1** (0.20 mM) with PhIO (1.5 equiv dissolved in trifluoroethanol (TFE)) followed by addition of HOTf (1 equiv) in MeCN at −40 °C. For all reactivity studies, **3** was generated by reacting **1** with 1.5 equiv PhIO (in TFE) followed by addition of 1 equiv of HOTf in MeCN at −40 °C or at 0 °C. **3-^{18}O** was prepared using $PhI^{18}O$ instead of $PhI^{16}O$. **3** can be generated in more than 95 % yield using other solvents such as acetone, TFE and also mixture of solvents such as acetonitrile:acetone (*v*/*v* = 1:9) and acetonitrile:butyronitrile (*v*/*v* = 1:2). For characterization techniques (such as EXAFS, MCD, EPR, and ^{1}H-NMR), higher concentration of **3** was prepared (up to 8.0 mM) in MeCN or mixture solvent depending on the requirement of technique used.

X-ray Crystallography. Single crystals of **1** and **2** were picked from the solutions using a nylon loop on (Hampton Research Co.) a copper plate mounted on a goniometer head in nitrogen cryosteam. Data collections were carried out at 100 K on a Bruker APEX-II CCD diffractometer equipped with a monochromator using a MoKα (λ = 0.71073 Å) incident beam. The CCD data were integrated and scaled using the Bruker-SAINT software package, and the structure was solved and refined using ShelXL.[66,67] All the non-hydrogen atoms were refined anisotropically. All hydrogen atoms were added to their geometrically ideal positions. The crystallographic data and selected bond distances and angles for **1**, and **2** are listed in SI, Tables S1 – S4 and Figure S2 and Figure S4. The X–ray crystallographic coordinates for structures reported here have been deposited at the Cambridge Crystallographic Data Centre (CCDC) with the deposition number, CCDC-2182967 for **1** and CCDC-2182968 for **2**.

Spin-State Determination of 1 and 2 by Evans Method. The spin states of **1** and **2** were obtained at room temperature by using the modified ^{1}H NMR method of Evans.[68–70] A sealed capillary (WILMAD® coaxial insert) tube with blank MeOD or acetone-d_6 solvent (containing 1.0% TMS) was placed into the normal NMR tubes containing 2.0 mM the complex solution in MeOD or acetone-d_6 (containing 0.1% TMS). The chemical shift of the TMS peak in the presence of the metal complexes were then compared with the TMS peak in the outer NMR tube. The magnetic moment was then calculated using the following equation,

$$\mu = 0.0618(\Delta \nu T / 2fM)^{1/2}$$

where oscillator frequency of the superconducting spectrometer in MHz is denoted as *f*, *T* stands for absolute temperature, molar concentration of the metal ion is denoted as *M*, and *v* represents the difference in frequency (Hz) between the two reference signals. ^{1}H NMR Evans method

allowed us to determine magnetic moment of complex **1** in MeOD and **2** in acetone-d_6 solvent. The spin state of **1** and **2** were found to be S_t = 0 and S_t = 1/2, respectively.

Kinetic Measurements. All the reactions were run in a 1.0 cm UV cuvette by monitoring UV-Vis spectral changes of reaction solutions. First-order rate constants for the oxidation of substrates by **3** were determined under pseudo-first-order conditions (e.g., [substrate]/[**3**] > 10) by fitting the decay of absorbance at 728 nm due to **3** in the oxidation of substrates by **3** in MeCN at −40 °C. The first-order plots were linear for three or more half-lives with the correlation coefficient of ρ > 0.99. The pseudo-first-order rate constants increased proportionally with the concentrations of substrates, from which second-order rate constants were determined. In the cases of stopped-flow data, the raw kinetic data were treated with KinetAsyst 3 (Hi-Tech Scientific) and Specfit/32 Global Analysis System software from Spectrum Software Associates. Reactions were run at least in triplicate, and the data reported represent the average values of these reactions. Kinetic isotope effect (KIE) values were determined by comparing the second-order rates obtained in the oxidation of xanthene-h_2 versus xanthene-d_2 by **3** in MeCN at 0 °C.

Nickel K-edge X-ray Absorption Spectroscopy. Nickel K-edge X-ray absorption spectroscopic data were collected on the HXMA beamline at the Canadian Light Source (Saskatoon, SA, Canada). Solutions of **1**, **2** and **3** (2.0 mM in acetonitrile) were injected between Kapton tape windows in aluminum sample holders and quickly frozen in liquid nitrogen. Data were collected at 20 K with sample temperatures maintained using an Oxford liquid He cryostat. Light was monochromatized using a Si(220) double crystal monochromator, which was detuned by 50% (80% for **3**) for harmonic rejection, and focused using a Rh mirror. Spectra were obtained in fluorescence mode using a 32-element solid-state Ge detector with a 3 micron cobalt filter placed between the sample and detector, and spectra were calibrated against the first inflection point of Ni-foil, which was simultaneously recorded with the data. EXAFS and XANES data for **3** were obtained in 10 eV steps in the pre-edge region (8133 – 8313 eV, 1 s integration time), 0.3 eV steps in the pre-edge region (8313 – 8363 eV, 3 s integration time), 1.0 eV steps in the edge region (8363 – 8433 eV, 3 s integration time), 2.0 eV steps in the near edge region (8433 – 8633 eV, 3 s integration time), and 0.05 k steps in the far edge region (8633 eV – 16.0 $Å^{-1}$, 3 s integration time). XANES data for **1** and **2** were obtained data were obtained in 10 eV steps in the pre-edge region (8133 – 8313 eV, 1 s integration time), 0.3 eV steps in the pre-edge region (8313 – 8363 eV, 3 s integration time), 1.0 eV steps in the edge region (8363 – 8433 eV, 3 s integration time) and 2.0 eV steps in the far edge region (8433 – 10 *k*, 3 s integration time. To avoid sample photoreduction the 1 × 1 mm beam spot was moved after every scan. Total fluorescence counts were maintained under 30 kHz, and a deadtime correction yielded no appreciable change to the data. The reported XANES spectra for **1** and **2** represent the averaged spectra from 3 data sets while the XANES and EXAFS spectra for **3** represents 10 individual data sets. Prior to data averaging each spectrum and detector channel was individually inspected for data quality. Although data were recorded to 16 $Å^{-1}$, the data were analyzed only from 2.0 – 13.0 $Å^{-1}$ owing to noise at high *k*. Data were subsequently processed and analyzed as previously reported using *EXAFS123, LARCH*, and *FEFF 9.4*.[71–73]

Product Analysis. Products produced in the oxidation of thioanisole and styrene by **3** in MeCN were analyzed by HPLC, GC and GC-MS. Thioanisole (10 mM) or styrene (10 mM) were added directly to a solution of **3** (1.0 mM) at −40 °C and then the mixture was stirred for 10 min. Methyl phenyl sulfoxide and benzaldehyde were obtained as the major product in the oxidation of thioanisole and styrene respectively by **3**. Product yields were determined by comparing the peak

areas of sample products in GC chromatograms against standard curves prepared with known authentic references using decane as an internal standard. Products formed in the oxidation of xanthene by **3** were analyzed by GC and GC−MS. Xanthone was obtained as a major product in the C–H bond activation reaction of xanthene by **3** under an Ar atmosphere. The nickel products formed in the reaction of **3** with thioanisole, styrene and 1-4-cyclohexadiene were analyzed by CSI-MS and EPR techniques. In all the reactions, Ni^{III} species were produced as a major product.

Conflicts of interest

There are no conflicts to declare.

Associated Content

Supporting Information Available: Structural and further spectroscopic characterization of **1** and **2**, further spectroscopic characterization of **3**, coordinates of DFT optimized structures, MCD VTVH fitting information, DFT calculated properties and reactivity of **3**.

Author Information

Corresponding Authors:

jshearer@trinity.edu

lehnertn@umich.edu

wwnam@ewha.ac.kr

ORCID:

Deepika Karmalkar: 0000-0001-7386-6989

Virginia A. Larson: 0000-0002-7094-6286

Deesha D. Malik: 0000-0001-7800-8852

Yong-Min Lee: 0000-0002-5553-1453

Mi Sook Seo: 0000-0003-3302-2508

Jin Kim: 0000-0003-4006-8897

Jason Shearer: 0000-0001-7469-7304

Nicolai Lehnert: 0000-0002-5221-5498

Wonwoo Nam: 0000-0001-8592-4867

Author Contributions

† D.G.K. and V.A.L. are co-first authors.

Acknowledgements

This work was supported by a grant from the National Science Foundation (CHE-1900380 to NL and JS). This work was also supported by the NRF of Korea through CRI (NRF-2021R1A3B1076539 to W.N.) and Basic Science Research Program (NRF-2020R1I1A1A01074630 to Y.-M.L. and NRF-2019R1I1A1A01055822 to M.S.S.). VAL acknowledges support from a University of Michigan Rackham Predoctoral Fellowship.

References

(1) Larson, V. A.; Battistella, B.; Ray, K.; Lehnert, N.; Nam, W. Iron and Manganese Oxo Complexes, Oxo Wall and Beyond. *Nat. Chem. Rev.* **2020**, *4*, 404–419. https://doi.org/10.1038/s41570-020-0197-9.

(2) Zhang, X. P.; Chandra, A.; Lee, Y. M.; Cao, R.; Ray, K.; Nam, W. Transition Metal-Mediated O–O Bond Formation and Activation in Chemistry and Biology. *Chem. Soc. Rev.* **2021**, *50*, 4804–4811. https://doi.org/10.1039/D0CS01456G.

(3) Armstrong, F. A. Why Did Nature Choose Manganese to Make Oxygen? *Philos. Trans. R. Soc. B Biol. Sci.* **2008**, *363*, 1263–1270. https://doi.org/10.1098/rstb.2007.2223.

(4) Riggs-Gelasco, P. J.; Price, J. C.; Guyer, R. B.; Brehm, J. H.; Barr, E. W.; Bollinger, J. M.; Krebs, C. EXAFS Spectroscopic Evidence for an Fe=O Unit in the Fe(IV) Intermediate Observed during Oxygen Activation by Taurine:α-Ketoglutarate Dioxygenase. *J. Am. Chem. Soc.* **2004**, *126*, 8108–8109. https://doi.org/10.1021/ja048255q.

(5) Solomon, E. I.; Heppner, D. E.; Johnston, E. M.; Ginsbach, J. W.; Cirera, J.; Qayyum, M.; Kieber-Emmons, M. T.; Kjaergaard, C. H.; Hadt, R. G.; Tian, L. Copper Active Sites in Biology. *Chem. Rev*. **2014**, *114*, 3659–3853. https://doi.org/10.1021/cr400327t.

(6) Solomon, E. I. Dioxygen Binding, Activation, and Reduction to H_2O by Cu Enzymes. *Inorg. Chem.* **2016**, *55*, 6364–6375. https://doi.org/10.1021/acs.inorgchem.6b01034.

(7) Quist, D. A.; Diaz, D. E.; Liu, J. J.; Karlin, K. D. Activation of Dioxygen by Copper Metalloproteins and Insights from Model Complexes. *J. Biol. Inorg. Chem.* **2017**, *22*, 253–288. https://doi.org/10.1007/s00775-016-1415-2.

(8) Borovik, A. S. Role of Metal-Oxo Complexes in the Cleavage of C-H Bonds. *Chem. Soc. Rev.* **2011**, *40*, 1870–1874. https://doi.org/10.1039/c0cs00165a.

(9) Chen, Z.; Yin, G. The Reactivity of the Active Metal Oxo and Hydroxo Intermediates and Their Implications in Oxidations. *Chem. Soc. Rev.* **2015**, *44*, 1083–1100.

(10) Ray, K.; Pfaff, F. F.; Wang, B.; Nam, W. Status of Reactive Non-Heme Metal-Oxygen Intermediates in Chemical and Enzymatic Reactions. *J. Am. Chem. Soc.* **2014**, *136*, 13942–13958.

(11) Guo, M.; Corona, T.; Ray, K.; Nam, W. Heme and Nonheme High-Valent Iron and Manganese Oxo Cores in Biological and Abiological Oxidation Reactions. *ACS Cent. Sci.* **2019**, *5*, 13–28. https://doi.org/10.1021/acscentsci.8b00698.

(12) Guo, M.; Lee, Y. M.; Fukuzumi, S.; Nam, W. Biomimetic Metal-Oxidant Adducts as Active Oxidants in Oxidation Reactions. *Coord. Chem. Rev.* **2021**, *435*, 213807. https://doi.org/10.1016/J.CCR.2021.213807.

(13) Paik, A.; Paul, S.; Bhowmik, S.; Das, R.; Naveen, T.; Rana, S. Recent Advances in First-Row Transition-Metal-Mediated C−H Halogenation of (Hetero)Arenes and Alkanes. *Asian J. Org. Chem.* **2022**, *11*, e202200060. https://doi.org/10.1002/AJOC.202200060.

(14) McEvoy, J. P.; Brudvig, G. W. Water-Splitting Chemistry of Photosystem II. *Chem. Rev.* **2006**, *106*, 4455–4483. https://doi.org/10.1021/CR0204294.

(15) Lewis, N. S.; Nocera, D. G. Powering the Planet: Chemical Challenges in Solar Energy

Utilization. *Proc. Natl. Acad. Sci. U. S. A.* **2006**, *103*, 15729–15735. https://doi.org/10.1073/pnas.0603395103.

(16) den boer, D.; Hetterscheid, D. G. H. Design Principles for Homogeneous Water Oxidation Catalysts Based on First–Row Transition Metals. *Curr. Opin. Electrochem.* **2022**, 101064. https://doi.org/10.1016/J.COELEC.2022.101064.

(17) Hocking, R. K. The Search for Intermediates Formed during Water-Oxidation Catalysis. *Chem. Catal.* **2021**, *1*, 248–250. https://doi.org/10.1016/J.CHECAT.2021.06.004.

(18) Xiao, D.; Gregg, J.; Lakshmi, K. V; Bonitatibus, P. J.; Xiao, D. ; Gregg, J. ; Lakshmi, K. V. ; Bonitatibus, P. J. Bio-Inspired Molecular Catalysts for Water Oxidation. *Catalysts* **2021**, *11*, 1068. https://doi.org/10.3390/catal11091068.

(19) Nocera, D. G. The Artificial Leaf. *Acc. Chem. Res.* **2012**, *45*, 767–776.

(20) Li, X.-X.; Cho, K. Bin; Nam, W. Electronic Properties and Reactivity Patterns of High-Valent Metal-Oxo Species of Mn, Fe, Co, and Ni. *Bull. Korean Chem. Soc.* **2021**, *42*, 1506–1512. https://doi.org/10.1002/BKCS.12389.

(21) Gray, H. B.; Winkler, J. R. Living with Oxygen. *Acc. Chem. Res.* **2018**, *51*, 1850–1857. https://doi.org/10.1021/acs.accounts.8b00245.

(22) Winkler, J. R.; Gray, H. B. Electronic Structures of Oxo-Metal Ions. *Struct. Bond.* **2012**, *142*, 17–28. https://doi.org/10.1007/430_2011_55.

(23) Sen, A.; Rajaraman, G. Can You Break the Oxo-Wall? A Multiconfigurational Perspective. *Faraday Discuss.* **2022**, *234*, 175–194. https://doi.org/10.1039/D1FD00072A.

(24) Koola, J. D.; Kochi, J. K. Nickel Catalysis of Olefin Epoxidation. *Inorg. Chem.* **1987**, *26*, 908–916.

(25) Kinneary, J. F.; Albert, J. S.; Burrows, C. J. Mechanistic Studies of Alkene Epoxidation Catalyzed by Nickel(II) Cyclam Complexes. Oxygen-18 Labeling and Substituent Effects. *J. Am. Chem. Soc.* **1988**, *110*, 6124–6129.

(26) Nagataki, T.; Tachi, Y.; Itoh, S. Ni^{II}(TPA) as an Efficient Catalyst for Alkane Hydroxylation with m-CPBA. *Chem. Commun.* **2006**, *38*, 4016–4018.

(27) Božović, A.; Feil, S.; Koyanagi, G. K.; Viggiano, A. A.; Zhang, X.; Schlangen, M.; Schwarz, H.; Bohme, D. K. Conversion of Methane to Methanol: Nickel, Palladium, and Platinum (d^9) Cations as Catalysts for the Oxidation of Methane by Ozone at Room Temperature. *Chem. - Eur. J.* **2010**, *16*, 11605–11610. https://doi.org/10.1002/chem.201000627.

(28) Shiota, Y.; Yoshizawa, K. Methane-to-Methanol Conversion by First-Row Transition-Metal Oxide Ions: ScO^+, TiO^+, VO^+, CrO^+, MnO^+, FeO^+, CoO^+, NiO^+, and CuO^+. *J. Am. Chem. Soc.* **2000**, *122*, 12317–12326. https://doi.org/10.1021/ja0017965.

(29) Qiu, Y.; Hartwig, J. F. Mechanism of Ni-Catalyzed Oxidations of Unactivated C(Sp3)-H Bonds. *J. Am. Chem. Soc.* **2020**, *142*, 19239–19248. https://doi.org/10.1021/JACS.0C09157.

(30) Nesterov, D. S.; Nesterova, O. V. Catalytic Oxidations with Meta-Chloroperoxybenzoic Acid (m-CPBA) and Mono-and Polynuclear Complexes of Nickel: A Mechanistic Outlook. *Catalysts* **2021**, *11*, 1148. https://doi.org/10.3390/catal11101148.

(31) Fukuzumi, S.; Cho, K. Bin; Lee, Y. M.; Hong, S.; Nam, W. Mechanistic Dichotomies in Redox Reactions of Mononuclear Metal–Oxygen Intermediates. *Chem. Soc. Rev.* **2020**, *49*, 8988–9027. https://doi.org/10.1039/D0CS01251C.

(32) Pfaff, F. F.; Heims, F.; Kundu, S.; Mebs, S.; Ray, K. Spectroscopic Capture and Reactivity of *S* = 1/2 Nickel(III)–Oxygen Intermediates in the Reaction of a Ni^{II}-Salt with *m*CPBA. *Chem. Commun.* **2012**, *48*, 3730–3732.

(33) Corona, T.; Pfaff, F. F.; Acuña-Parés, F.; Draksharapu, A.; Whiteoak, C. J.; Martin-Diaconescu, V.; Lloret-Fillol, J.; Browne, W. R.; Ray, K.; Company, A. Reactivity of a Nickel(II) Bis(Amidate) Complex with *Meta*-Chloroperbenzoic Acid: Formation of a Potent Oxidizing Species. *Chem. - Eur. J.* **2015**, *21*, 15029–15038. https://doi.org/10.1002/chem.201501841.

(34) Bok, K. H.; Lee, M. M.; You, G. R.; Ahn, H. M.; Ryu, K. Y.; Kim, S.-J.; Kim, Y.; Kim, C. Synthesis, Characterization, and Catalytic Activities of A Nickel(II) Monoamido-Tetradentate Complex: Evidence For Ni^{III}-Oxo and Ni^{IV}-Oxo Species. *Chem. - Eur. J.* **2017**, *23*, 3117–3125. https://doi.org/10.1002/chem.201605157.

(35) Cho, J. H.; Kim, S.; Lee, H. I. Peroxidase-like Activity of an Azamacrocyclic Ni(II) Complex. *Bull. Korean Chem. Soc.* **2022**, *43*, 417–420. https://doi.org/10.1002/BKCS.12493.

(36) Farhat, R.; Dhainy, J.; Halaoui, L. I. Oer Catalysis at Activated and Codeposited Nife-Oxo/Hydroxide Thin Films Is Due to Postdeposition Surface-Fe and Is Not Sustainable without Fe in Solution. *ACS Catal.* **2020**, *10*, 20–35. https://doi.org/10.1021/acscatal.9b02580.

(37) Kim, S.; Jeong, H. Y.; Kim, S.; Kim, H.; Lee, S.; Cho, J.; Kim, C.; Lee, D. Proton Switch in the Secondary Coordination Sphere to Control Catalytic Events at the Metal Center: Biomimetic Oxo Transfer Chemistry of Nickel Amidate Complex. *Chem. - Eur. J.* **2021**, *27*, 4700–4708. https://doi.org/10.1002/CHEM.202005183.

(38) Hu, J.; Li, Y.; Zou, Y.; Lin, L.; Li, B.; Li, X. yan. Transition Metal Single-Atom Embedded on N-Doped Carbon as a Catalyst for Peroxymonosulfate Activation: A DFT Study. *Chem. Eng. J.* **2022**, *437*, 135428. https://doi.org/10.1016/J.CEJ.2022.135428.

(39) Li, L.; Beckers, H.; Stüker, T.; Lindič, T.; Schlöder, T.; Andrae, D.; Riedel, S. Molecular Oxofluorides OMFn of Nickel, Palladium and Platinum: Oxyl Radicals with Moderate Ligand Field Inversion. *Inorg. Chem. Front.* **2021**, *8*, 1215–1228. https://doi.org/10.1039/D0QI01151G.

(40) Lee, H.; Wu, X.; Sun, L. Homogeneous Electrochemical Water Oxidation at Neutral PH by Water-Soluble NiII Complexes Bearing Redox Non-innocent Tetraamido Macrocyclic Ligands. *ChemSusChem* **2020**, *13*, 3277–3282.

(41) $\Delta r = \pi(2\Delta k)^{-1}$

(42) In addition to the innersphere shells, three outersphere Ni-C shells were included to account for the outersphere scattering to the ligand framework.

(43) Stephens, P. J. Magnetic Circular Dichroism. *Adv. Chem. Phys.* **1976**, *35*, 197–264.

(44) Solomon, E. I.; Pavel, E. G.; Loeb, K. E.; Campochiaro, C. Magnetic Circular Dichroism Spectroscopy as a Probe of the Geometric and Electronic Structure of Non-Heme Ferrous Enzymes. *Coord. Chem. Rev.* **1995**, *144*, 369–460.

(45) Neese, F.; Solomon, E. I. MCD C-Term Signs, Saturation Behavior, and Determination of Band Polarizations in Randomly Oriented Systems with Spin S > 1/2. Applications to S = 1/2 and S = 5/2. *Inorg. Chem.* **1999**, *38*, 1847–1865.

(46) Lehnert, N.; DeBeer George, S.; Solomon, E. I. Recent Advances in Bioinorganic Spectroscopy. *Curr. Opin. Chem. Biol.* **2001**, *5*, 176–187.

(47) Lehnert, N. Elucidating Second Coordination Sphere Effects in Heme Proteins Using Low-Temperature Magnetic Circular Dichroism Spectroscopy. *J. Inorg. Biochem.* **2012**, *110*, 83–93.

(48) Collins, T. J.; Powell, R. D.; Slebodnick, C.; Uffelman, E. S. Stable Highly Oxidizing Cobalt Complexes of Macrocyclic Ligands. *J. Am. Chem. Soc.* **1991**, *113*, 8419–8425. https://doi.org/10.1021/ja00022a033.

(49) Chanda, A.; Popescu, D. L.; de Oliveira, F. T.; Bominaar, E. L.; Ryabov, A. D.; Münck, E.; Collins, T. J. High-Valent Iron Complexes with Tetraamido Macrocyclic Ligands: Structures, Mössbauer Spectroscopy, and DFT Calculations. *J. Inorg. Biochem.* **2006**, *100*, 606–619. https://doi.org/10.1016/J.JINORGBIO.2005.12.016.

(50) Popescu, D.-L.; Chanda, A.; Stadler, M.; de Oliveira, F. T.; Ryabov, A. D.; Münck, E.; Bominaar, E. L.; Collins, T. J. High-Valent First-Row Transition-Metal Complexes of Tetraamido (4*N*) and Diamidodialkoxido or Diamidophenolato (2*N*/2*O*) Ligands: Synthesis, Structure, and Magnetochemistry. *Coord. Chem. Rev.* **2008**, *252*, 2050–2071. https://doi.org/10.1016/J.CCR.2007.11.006.

(51) Luo, Y.-R. *Handbook of Bond Dissociation Energies in Organic Compounds*; CRC press, 2002.

(52) Kwon, Y. M.; Lee, Y.; Schmautz, A. K.; Jackson, T. A.; Wang, D. C–H Bond Activation by a Mononuclear Nickel (IV)-Nitrate Complex. *J. Am. Chem. Soc.* **2022**, *144*, 12072–12080.

(53) Wang, S.; Ma, P.; Shaik, S.; Chen, H. Valence-Inverted States of Nickel(II) Complexes Perform Facile C–H Bond Activation. *J. Am. Chem. Soc.* **2022**, *144*, 14607–14613. https://doi.org/10.1021/JACS.2C03835.

(54) Saltzman, H.; Sharefkin, J. G. Organic Syntheses; Wiley: New York, 1973; pp 658–659.

(55) Goldsmith, C. R.; Jonas, R. T.; Stack, T. D. P. C-H Bond Activation by a Ferric Methoxide Complex: Modeling the Rate-Determining Step in the Mechanism of Lipoxygenase. *J. Am. Chem. Soc.* **2002**, *124*, 83–96. https://doi.org/10.1021/ja016451g.

(56) M. J. Frisch H. B. Schlegel, G. E. Scuseria, M. A. Robb, J. R. Cheeseman, G. Scalmani, V. Barone, B. Mennucci, G. A. Petersson, H. Nakatsuji, M. Caricato, X. Li, H. P. Hratchian, A. F. Izmaylov, J. Bloino, G. Zheng, J. L. Sonnenberg, M. Hada, M. Ehara, K, G. W. T. Gaussian 09. *Gaussian*. Gaussian, Inc.: Wallingford CT 2009.

(57) Becke, A. D. Density-Functional Exchange-Energy Approximation with Correct Asymptotic-Behavior. *Phys. Rev. A* **1988**, *38*, 3098–3100. https://doi.org/10.1103/PhysRevA.38.3098.

(58) Becke, A. D. Density-Functional Thermochemistry. III. The Role of Exact Exchange. *J. Chem. Phys.* **1993**, *98*, 5648–5652. https://doi.org/10.1063/1.464913.

(59) Lee, C.; Yang, W.; Parr, R. G. Development of the Colle-Salvetti Correlation-Energy Formula into a Functional of the Electron Density. *Phys. Rev. B* **1988**, *37*, 785–789.

(60) Perdew, J. P. Density-Functional Approximation for the Correlation-Energy of the Inhomogeneous Electron-Gas. *Phys. Rev. B* **1986**, *33*, 8822–8824. https://doi.org/10.1103/PhysRevB.33.8822.

(61) Adamo, C.; Barone, V. Toward Reliable Density Functional Methods without Adjustable Parameters: The PBE0 Model. *J. Chem. Phys.* **1999**, *110*, 6158–6170. https://doi.org/10.1063/1.478522.

(62) Tao, J. M.; Perdew, J. P.; Staroverov, V. N.; Scuseria, G. E. Climbing the Density Functional Ladder: Nonempirical Meta–Generalized Gradient Approximation Designed for Molecules and Solids. *Phys. Rev. Lett.* **2003**, *91*, 146401. https://doi.org/10.1103/PhysRevLett.91.146401.

(63) Staroverov, V. N.; Scuseria, G. E.; Tao, J.; Perdew, J. P. Comparative Assessment of a New Nonempirical Density Functional: Molecules and Hydrogen-Bonded Complexes. *J. Chem. Phys.* **2003**, *119*, 12129-12137. https://doi.org/10.1063/1.1626543.

(64) Staroverov, V. N.; Scuseria, G. E.; Tao, J.; Perdew, J. P. Erratum: "Comparative Assessment of a New Nonempirical Density Functional: Molecules and Hydrogen-Bonded Complexes" [J. Chem. Phys. 119, 12129 (2003)]. *J. Chem. Phys.* **2004**, *121*, 11507. https://doi.org/10.1063/1.1795692.

(65) Neese, F. Software Update: The ORCA Program System, Version 4.0. *Wiley Interdiscip. Rev. Mol. Sci.* **2018**, *8* (1), e1327. https://doi.org/10.1002/wcms.1327.

(66) GM Sheldrick. Crystal Structure Refinement with SHELXL. *Acta Crystallogr.* **2015**, *C71*, 3–8.

(67) Spek, A. L. Structure Validation in Chemical Crystallography. *Acta Crystallogr. Sect. D Biol. Crystallogr.* **2009**, *65*, 148–155.

(68) Evans, D. F. The Determination of the Paramagnetic Susceptibility of Substances in Solution by Nuclear Magnetic Resonance. *J. Chem. Soc.* **1959**, 2003–2005.

(69) Loliger, J.; Scheffold, R. Paramagnetic Moment Measurements by Nmr. A Micro Technique. *J. Chem. Educ.* **1972**, *49*, 646.

(70) Evans, D. F.; Jakubovic, D. A. Water-Soluble Hexadentate Schiff-Base Ligands as Sequestrating Agents for Iron (III) and Gallium (III). *J. Chem. Soc. Dalt. Trans.* **1988**, 2927–2933.

(71) Rehr, J. J.; Kas, J. J.; Vila, F. D.; Prange, M. P.; Jorissen, K. Parameter-Free Calculations of X-Ray Spectra with FEFF9. *Phys. Chem. Chem. Phys.* **2010**, *12*, 5503–5513.

(72) Scarrow, R. C.; Strickler, B. S.; Ellison, J. J.; Shoner, S. C.; Kovacs, J. A.; Cummings, J. G.; Nelson, M. J. X-Ray Spectroscopy of Nitric Oxide Binding to Iron in Inactive Nitrile Hydratase and a Synthetic Model Compound. *J. Am. Chem. Soc.* **1998**, *120*, 9237–9245.

(73) Newville, M. Larch: An Analysis Package for XAFS and Related Spectroscopies. In *Journal of Physics: Conference Series*; IOP Publishing, 2013; Vol. 430, p 12007.

For Table of Contents only: